University of Alberta

Sliding-Mode Control of Pneumatic Actuators for Robots and Telerobots

by

Sean Edward Hodgson

A thesis submitted to the Faculty of Graduate Studies and Research
in partial fulfillment of the requirements for the degree of

Masters of Science

in

Control Systems

Department of Electrical and Computer Engineering

This thesis is dedicated to Jennifer Liggett, Linda Hodgson, and Geoff Hodgson for their unconditional love and support throughout the course of my M.Sc.

Abstract

For robotic systems that use pneumatic actuators with on/off solenoid valves, sliding-mode control laws for precise position control and low switching (open/close) activity of the valves are presented. A pneumatic actuator has two chambers with a total of four on/off solenoid valves. Thus, there are sixteen possible combinations for the valves' on/off positions. Only seven of these sixteen "operating modes" are considered both functional and unique. While previous work has focused on three-mode closed-loop control of such an actuator, this thesis extends the three-mode control to seven-mode control. This thesis also extends the application from the position control of a single robot to the bilateral control of a telerobot.

We introduce and compare two novel seven-mode controllers for a pneumatic actuator. The first is a sliding-mode controller utilizing a switching function that is a function of the system states. The second is a sliding-mode, pulse-width-modulation (PWM) controller utilizing a time-averaged model of the open-loop system. Both controllers minimize the tracking error by employing the operating modes that have the necessary and sufficient amounts of drive energy and, thus, involve reduced switching activity while maintaining satisfactory tracking performance. The performance of the proposed control design is experimentally verified on a single pneumatic actuator.

Also, the seven-mode position control is extended to force control to make seven-mode teleoperation control possible. Experimental verification on a pair of pneumatic actuators utilizing position-position based and force-position based teleoperation control to verify the validity of our theoretical results. Overall, it is found that leveraging the additional modes of operation leads to more efficient and smoother control in both the single-actuator and the dual-actuator teleoperated pneumatic systems.

Acknowledgements

First and foremost, I would like to express my sincere gratitude to my supervisor Dr. Mahdi Tavakoli for his continuous encouragement and guidance throughout my M.Sc study and research. He is always accessible and willing to help his students with their research. As a result, research life has became smooth and rewarding for me.

Secondly, I would like to thank the Laboratoire Ampère for providing funding and lab equipment. I am also grateful for the professors and students at the University of Lyon. In particular: Dr. Minh-Tu Pham, Dr. Arnaud Leleve, and Minh-Quyen Le for their useful discussions, suggestions, and advice.

I would like to thank the many people who have taught me mathematics: my high school science teachers (especially Norman Stonehouse and Richard Dybvig), my undergraduate teachers at University of Saskatchewan (especially Robert Johanson) for their kind assistance with writing letters, helping with various applications and so on. I would also like to extend my personal thanks to Jeanne Smith for always encouraging me to strive further.

I thank my fellow lab-mates in the Telerobotic and Biorobotic Systems group for providing a stimulating and fun environment in which to learn and grow. I am especially grateful to Ali Jazayeri, Meaghan Bowthorpe, Arefeh Boroomand, Alireza Mohammadi, and Matthew Dyck. They have all provided useful discussions and insights for my day to day efforts.

My sincere thanks also goes to my colleagues at Ultra-Electronics and Cobham Tracking and Locating for offering me the work experience and mentorship to develop my industrial design skills. I would especially like to thank: Don Dinn, Andrew Hanlon, Adam Pearce, Craig Hillis, Evan Locke, Colin Frame, Francis Dompier, Chris Oickle, Paul Arsenault, and Mark Gidney. The experience and wisdom they have shared with me, has allowed me to take a practical look at all future engineering design challenges.

Last but not least, I would like to thank my family for all their love and encouragement. For my parents who raised me, taught me, and supported me in all my pursuits. And most of all for my loving, encouraging, and patient girlfriend Jennifer Liggett whose faithful support during the final stages of this M.Sc is so appreciated. Thank you.

Contents

List of Figures

List of Tables

List of Abbreviations

BIBO Bounded input bounded output

Const Constant

DOF   Degree of freedom

LHS   Left hand side

LVDT Linear variable differential transformer

MR   Magnetic resonance

MRI   Magnetic resonance imaging

PWM   Pulse-width-modulation

RHS   Right hand side

RMS   Root mean square

SMC   Sliding-mode control

TE   Tracking Error

VSC   Variable structure control

Chapter 1

Introduction

1.1 Merits and Applications of Pneumatic Actuators

Modern robotic systems have enabled operation in environments that are difficult or hazardous for the human to reach or operate in. In robot-assisted surgery, for instance, the surgical robot may be required to work under strong magnetic fields such as inside a magnetic resonance imaging (MRI) scanner. An MRI scanner affords pictures with high resolution and contrast, providing surgeons with a patient's three-dimensional visualization [21] in a nearly real-time manner [35]. Robot-assisted surgery under MRI has the advantage that it can direct the surgical tools to targets not normally visible to the surgeon. Also, the immediate visual feedback during the operation makes the surgery more efficient as the patient does not have to leave the operating room for diagnostic testing.

Despite these benefits, magnetic resonance (MR) images are obtained through the use of strong and precise magnetic fields. Thus, no ferromagnetic material is allowed inside the MRI. The presence of any ferromagnetic material in the actuators, as is the case in electric motors, of the surgical robot will generate noises that make it difficult to obtain precise MR images [21]. If electric motors are to be used as actuators in MRI-compatible robots, the motors need to be placed far away from the magnetic field and the surgical site [12], creating many design complications. This represents a severe design limitation for surgical robots that are to work under MRI guidance. To date, there is no MRI-compatible surgical robot available; the Intuitive Surgical Inc's da Vinci system – the only clinically-approved and commercially-available surgical robot – is not MRI compatible [16].

Alternatively, it is possible to use pneumatic actuators to drive the surgical robots [41]. This is because pneumatic actuators can be used directly in the magnetic field and are thus completely MRI-compatible [8]. Therefore, in this thesis, we seek to study the control of pneumatic actuators for applications in robotic and telerobotic systems.

An example application for pneumatic-actuated and thus MR-compatible robots is the treatment of prostate cancer via prostate brachytherapy, which involves the delivery of radioactive seeds to the prostate via a needle. In brachytherapy, the accuracy of radioactive seed placement highly influences the clinical outcome of the treatment [24]. Improving

seed placement accuracy in prostate brachytherapy would reduce the incidence of relapse of cancer, thus improving the overall results of the treatment. Arguably, the best imaging of the prostate would be attained utilizing MRI [23]. Thus, the use of MRI with pneumatically-controlled actuators for seed placement has the potential to improve the accuracy of the seed placement.

A pneumatic actuator can increase seed placement accuracy for another reason as well. While current needle insertion methods involve gradually pushing the needle into the prostate, there is supporting research to suggest that insertion with a certain, well-defined amount of momentum (initial velocity) can reduce needle deflection (and thus seed misplacement) when compared to methods currently used [11]. Thus, the high ratio of power to weight in pneumatic systems also makes them an ideal candidate from the perspective of this high-velocity insertion approach.

In addition to being inert to magnetic fields, pneumatic actuators offer many advantages for positioning applications such as low maintenance cost, high power-to-weight ratio, cleanliness, and safety [25]. However, they suffer from common drawbacks including friction and sensitivity of the actuator dynamics to load and piston position along the cylinder stroke [7]. Also, from a control perspective, controlling a pneumatic actuator is a challenge because the system dynamics are highly nonlinear [38].

To control the input air flow in a pneumatic actuator, some pneumatic systems have utilized servo-valve actuators [15]. These valves allow for a continuous change of the input mass flow rate. However, servo-valve actuators are costly due to the precision machining required in their manufacturing. A low-cost alternative to a servo-valve is the on/off solenoid valve, which has as a result found widespread applications. Control methods to compensate for the nonlinearities of servo-valve actuated pneumatic systems have been reported [7, 38, 29, 14]. The difficulty is that the nonlinear nature of a pneumatic actuator is exacerbated when it uses on/off solenoid valves instead of servo-valves. In this case, precise control is difficult due to the discrete-input nature of the system.

Past research has addressed solenoid-valve pneumatic system control via pulse width modulation (PWM) [17, 1, 31, 33]. Using time-averaging, a PWM input with a sufficiently high frequency can approximate the continuous input properties of a servo-valve [29]. While there has been efforts to approximate the nonlinear dynamics of a solenoid-valve system as an equivalent linear system [25], the highly nonlinear nature of the system precludes the use of linear controllers.

It is possible to perform nonlinear model averaging on the nonlinear solenoid-valve system followed by PWM/sliding-mode control of the averaged nonlinear systems [29]. It is also possible to directly use sliding-mode control on the nonlinear solenoid-valve systems [18]. Sliding-mode control is a form of variable structure nonlinear control that alters the dynamics of the system by employing high-frequency switching control [36, 37]. Sliding-mode control can account for the nonlinearities of the system as well as its dynamic uncertainties

[18].

1.2 Operating Modes of a Solenoid-Valve Actuator

In this thesis, we consider a pneumatic actuator to be comprised of two chambers as shown in Figure 1.1. Each chamber has two solenoid valves, each of which can be either closed, connected to a compressed air supply (source pressure), or connected to exhaust (atmosphere pressure). With four solenoid valves, it appears that there would be a total of sixteen discrete modes for the actuator at any given time. However, since we cannot have a chamber connected to pressure and exhaust at the same time, only nine discrete modes exist. If we assume the three modes in which both chambers are closed, both chambers are venting, and both chambers are pressurizing are functionally very similar (which is true under the no load case), then the system has a total of seven unique discrete modes (we will later see this in more detail in Table 2.1).

A central idea in this thesis is that a sliding-mode controller can force the open-loop system to transition between these discrete operating modes, which were defined directly from the state of the on/off solenoid valves, with the transition between the modes being decided based on the current tracking error. In [18], three discrete modes are considered for a two-chamber solenoid-valve actuator similar to the one shown in Figure 1.1:

- Push and Pull (chamber P connected to supply pressure and chamber N connected to exhaust pressure)

- Pull and Push (chamber P connected to exhaust pressure and chamber N connected to supply pressure)

- Closed and Closed (both chambers' valves closed)

One of the contributions of this thesis is to expand the three-mode open-loop model of [18] into a seven-mode open-loop model. The new system has four extra modes, which facilitate the use of optimal amounts of drive energy for satisfactory positioning precision and reduced valve switching (open/close) activity. These four additional modes considered for the two-chamber actuator are:

- Push and Close (chamber P connected to supply pressure and chamber N is closed)

- Pull and Close (chamber P connected to exhaust pressure and chamber N is closed)

- Close and Push (chamber P is closed and chamber N is connected to supply pressure)

- Close and Pull (chamber P is closed and chamber N is connected to exhaust pressure)

Due to one chamber being closed, each of the above four modes involves a reduced amount of drive energy (and piston acceleration) as compared to the original three modes.
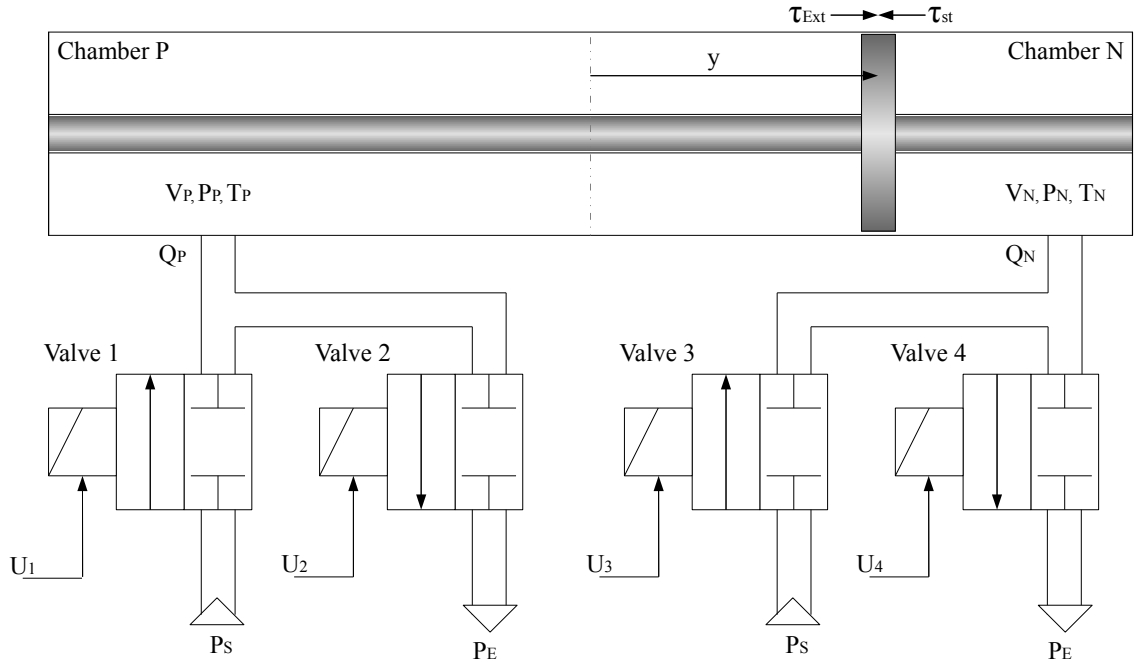
Figure 1.1: Electro-pneumatic system with 4 on/off solenoid valves.

This can allow for the delivery of optimal amounts of drive energy to the actuator, thus enabling more subtle adjustments of the piston position. By making fine position adjustments and thus avoiding piston overshoot, fewer valve switches will be required. The result is improved positioning accuracy and reduced switching activity for the controlled system.

Another contribution of this paper compared to the 3-mode design is in terms of providing design guidelines for the selection of threshold values used by the sliding controller to decide when to switch between the discrete operating modes of the open-loop system. The controller will use these thresholds for transition from one mode to another mode based on the full states of the system: the piston position, velocity, and acceleration as well as the chamber pressures; we will later see why the piston acceleration is also a state of this system. By optimizing these transition thresholds, we can decrease the switching activity of the on/off solenoid valves, which lengthens their operating lifespan.

1.3   Organization of the Thesis

The organization of this thesis is as follows:

- *Chapter 1. Introduction:* In this chapter, the background of solenoid-valve pneumatic systems and their main design approaches are introduced at a high level. The seven discrete modes of operation are illustrated.

- *Chapter 2. Background and System Model:* In this chapter, the principles of sliding-mode control are reviewed. A brief historical overview of teleoperation systems is also

presented and the system models of pneumatic actuators are presented.

- *Chapter 3. Sliding-Mode Control of a Single Pneumatic Actuator:* The sliding-mode control of a single pneumatic actuator is presented in this chapter. The seven-mode control of the system is developed as well as a method for selecting various parameters that decide the transition between modes. The experimental results for the seven-mode control model are presented.

- *Chapter 4. Sliding-Mode Control of a Teleoperator with Two Pneumatic Actuators:* In this chapter, the sliding-mode control is used inside a two-channel teleoperation system. The position-position based and force-position based teleoperation architectures are investigated both theoretically and experimentally.

- *Chapter 5. Model-Based Pulse-Width-Modulated Sliding-Mode Control*: A model-based, sliding-mode control is developed on the basis of PWM operation after approximating the discrete-input solenoid-valve system as a nonlinear continuous-input system. This method is examined both theoretically and experimentally. A stability proof for the single actuator case is presented and experimental results for the single actuator position control and force-position based teleoperation control are presented.

- *Chapter 6. Conclusions and Future Research:* Concluding remarks as well as potential future research directions are presented in this chapter.

Chapter 2

Background and System Model

In this chapter, the principles of sliding-mode control are reviewed. A brief historical overview of teleoperation systems is also presented and the system models of pneumatic actuators are presented.

2.1 Sliding-Mode Control Theory

In this section, we will present a brief overview of the theory behind sliding-mode control (SMC). For a complete review, please refer to [10, 27, 32, 40].

Variable structure control (VSC) systems are characterized by a suite of feedback control laws and a decision rule. The decision rule, also known as the switching function, has as its input some measure of the current system behaviour and produces as an output the particular feedback controller that should be used at that instant in time [27]. Variable structure control is a form of discontinuous nonlinear control and encompasses sliding-mode control.

In SMC, the multiple feedback control laws are designed so that trajectories always move towards an adjacent region with a different control structure, and so the trajectory will not exist entirely within one control structure. SMC is designed to drive and constrain the system states to lie within a particular neighbourhood of the switching function.

The system will "slide" along the subspace until it comes to a rest at a desired equilibrium. Thus, SMC allows the dynamic system behaviour to be shaped by the choice of the switching function [40].

2.1.1 Theory

Consider the single-input dynamic system

$$x^{(n)} = f(x) + g(x)u \tag{2.1}$$

Let $\tilde{x} = x - x_d$ be the tracking error of the state variable x. Let us define the time-varying

surface S in the state-space R^n by the scalar equation $S = 0$, where

$$S = (\frac{d}{dt} + \omega)^{n-1}\tilde{x} \tag{2.2}$$

and ω is a strictly positive constant. For instance if $n = 3$,

$$S = \ddot{\tilde{x}} + 2\omega\dot{\tilde{x}} + \omega^2\tilde{x} \tag{2.3}$$

meaning that S is a weighted sum of position error, velocity error, and acceleration error.

Given an initial condition of $x = x_d$, the problem of tracking is equivalent to that of remaining on the surface S for all $t > 0$; indeed $S = 0$ represents a linear differential equation whose unique solution is $\tilde{x} = 0$. Thus, the problem of tracking the n-dimensional vector x_d can be reduced to that of keeping the scalar quantity S at zero. More precisely, the problem of tracking the n-dimensional vector x_d can in effect be replaced by a first-order stabilization problem in S. Indeed, since S is a function $\tilde{x}^{n-1}$, see (2.2), we only need to differentiate S once for the input u to appear [32].

The simplified first-order problem of keeping the scalar S at zero can now be achieved by choosing the control law u from (2.1) such that

$$\frac{1}{2}\frac{d}{dt}S^2 \leq -\eta|S| \tag{2.4}$$

where η is a strictly positive constant. This law essentially states that the squared "distance" to the surface, as measured by S^2, decreases along all system trajectories. This condition is known as the reaching condition. The system constrained to a neighborhood around $S = 0$ is referred to as a "sliding surface", and the system's behavior once on the surface is called the "sliding regime" or the "sliding mode."

Another interesting aspect of being restricted to the sliding mode is that, once on it, the system trajectories are defined by the equation of the set itself, namely

$$(\frac{d}{dt} + \omega)^{n-1}\tilde{x} = 0 \tag{2.5}$$

Therefore, assuming ω is a positive constant and the system is not initially at equilibrium, $\tilde{x} \neq 0$, when the system is confined to the sliding mode the error $\tilde{x}$ will asymptotically approach zero. In other words, the sliding surface is both a place and a set of dynamics [32].

Now, assuming that the system is not initially on the sliding mode ($S \neq 0$), if the control has been selected such that condition (2.4) has been met, the surface $S = 0$ will nonetheless be reached in a *finite time* less than t_{reach} where

$$t_{reach} \leq \frac{|S_{t=0}|}{\eta} \tag{2.6}$$

See Figure 2.1 for the different phases of SMC.
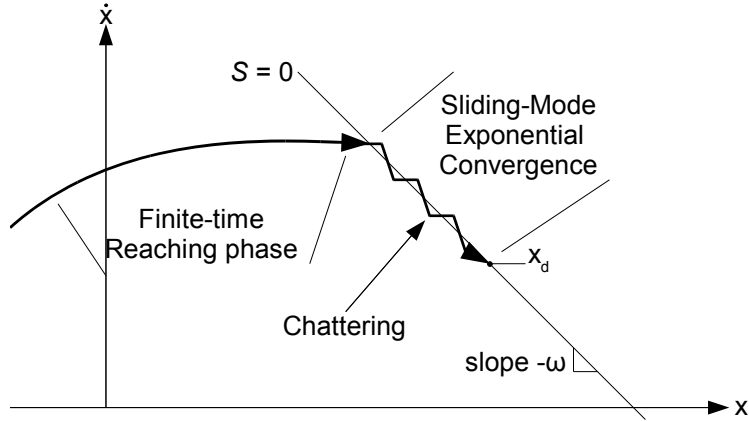
Figure 2.1: Sliding-mode control phases.

2.1.2 Direct Control Example

Sliding-Mode control is well recognized as a tool utilized to design robust controllers for complex high-order nonlinear dynamic plants operating under uncertain conditions. Consider the example of a second-order system with bang-bang control and sliding mode defined by the following equations from [36]:

$$\ddot{x} + a_2\dot{x} + a_1 x = u, \qquad u = -M\text{sign}(s), \qquad s = cx + \dot{x} \tag{2.7}$$

Here, M, c, a_1, and a_2 are constants. It follows from the analysis of the $(\dot{x}, x)$ state plane in Figure 2.2 that, in the neighborhood of segment mn on the switching line $s = 0$, the trajectories run in opposite directions, which leads to the appearance of a sliding mode along this line. While the system is constrained to a neighborhood around the switching line equation s = 0, the system dynamics may be treated as the following motion

$$cx + \dot{x} = 0 \tag{2.8}$$

with solutions that only depend on the slope c and are invariant to bounded variations of the plant parameters and bounded external disturbances. This is what was referred to in Section 2.1.1 by the switching function being both a place and a set of dynamics [32]. This causes the closed-loop system to become insensitive to the uncertainties of the controlled plant.

2.1.3 Chattering

The issue with sliding-mode control via a direct implementation of the switching control laws is chattering. Chattering, which can be observed in Figure 2.1, is small perturbation from the sliding-mode after it has been reached. Even with a perfect relay control that
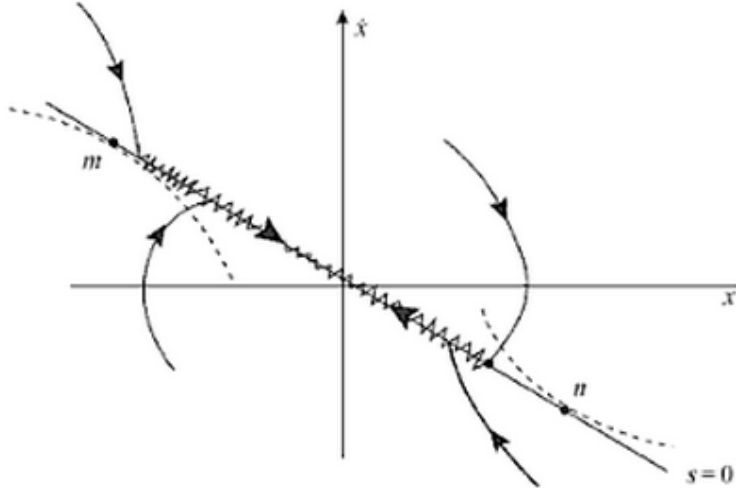
Figure 2.2: Second-order relay system.

can switch with infinite speed, this chattering effect can still be observed as the high-frequency switching can excite high frequency dynamics neglected in the course of modeling the system.

In general, chattering must be eliminated for the controller to perform properly. This can be achieved by smoothing out the control discontinuity in a thin boundary layer (see Figure 2.3) neighboring the switching surface. For our system, we have a discontinuous control input; however, it would be possible to implement an approximation of it as a continuous control input system utilizing PWM operation.

2.2 Historical Overview of Teleoperation Systems

Teleoperation aims to allow humans to sense/manipulate environments that are normally unavailable for a person to directly interact with. A master-slave teleoperation system comprises of a master robot controlled by the human operator and a slave robot that follows the movements of the master robot. The interaction between the human, the master and slave robots, and the environment leads to control design challenges especially for systems that require a very high level of fidelity (i.e., accurate transmissions of the environment properties to the human operator). Bilateral teleoperation systems have been developed for a variety of applications ranging from telesurgery to space exploration [28, 26, 34, 2, 14]. Below, we will present a brief history of teleoperation systems. For a complete review, please refer to [9, 4, 19, 30].

The first master-slave teleoperator was developed by Raymond C. Goertz to handle hazardous radioactive materials at the Argonne National Laboratory in 1945. This system underwent improvements in 1954 when electrical servomechanisms replaced the direct me-

(a) phase portrait

(b) continuous control

(c) discontinuous control
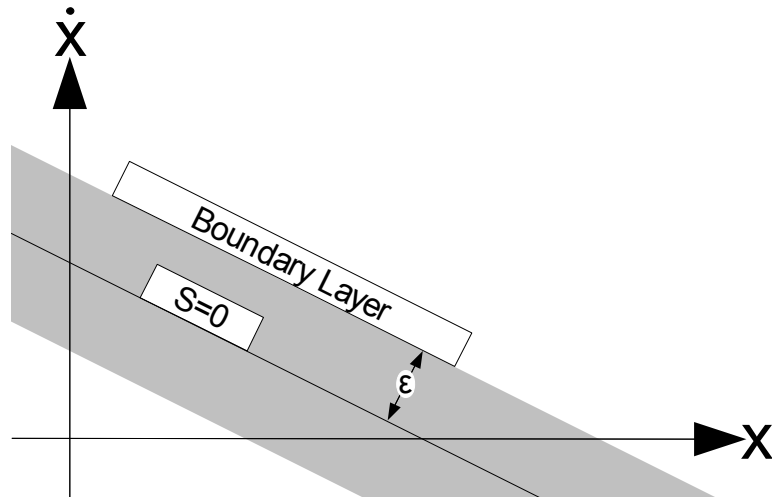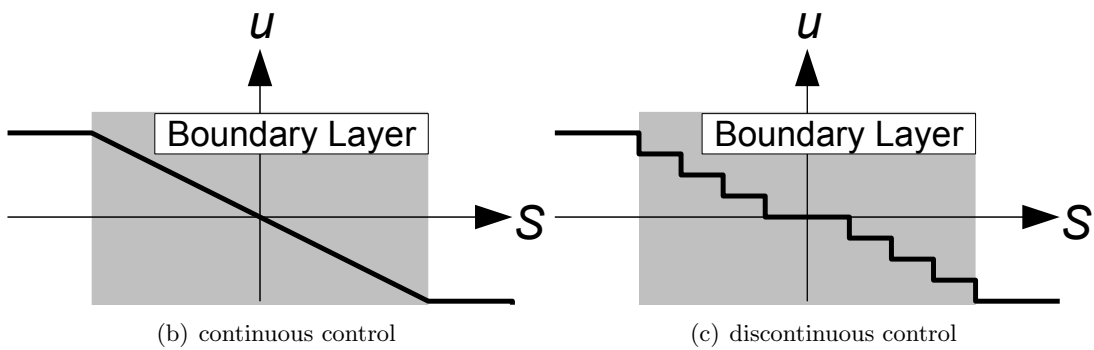
Figure 2.3: Sliding-mode boundary layer.

chanical tape and cable linkages, and closed circuit cameras were introduced so that the operator could be further away from the slave site [30].

As the race for the moon began in the early 1960's, the distance and the resulting time delay increased significantly. As a result, research into the effect of fixed or variable time delays on teleoperation systems was needed. In 1967, supervisory control was first introduced as a means to compensate for the time delay in a teleoperation systems. Supervisory control is based on the premise that high level commands are issued by the human operator, and the slave control system utilizes a certain level of autonomy to complete those commands [5].

In 1982, the Central Research Laboratory developed the first telerobotic system that realized force feedback while also separating the master and slave robots' electronics [19]. In the 1980's and 1990's, the interest re-focused around the space, medical, and underwater applications. The development of such systems was accelerated by the ever increasing computer power and novel hand controllers (joysticks) that could be used as the master robot. In 2001, a surgeron in New York (USA) conducted the first transatlantic telesurgery using the ZEUS system (from Computer Motion Inc.) to demonstrate the usefulness of telerobotic systems by performing a laparoscopic cholecystectomy on a patient in Strasbourg (France). This system did not include force feedback for the surgeon, however.

2.3 Single Pneumatic Actuator Model

In this section, we derive the open-loop model of a symmetric pneumatic actuator including its on/off solenoid valves as shown in Figure 1.1. It is because, in this thesis, we will work on the pneumatic actuator comprised of two chambers in Figure 1.1. Each chamber is connected to two solenoid valves. To describe the air flow dynamics in a cylinder, we assume that:

- Air is an ideal gas and its kinetic energy is negligible in the chambers,

- The pressure and the temperature are homogeneous in each chamber,

- The evolution of the gas in each chamber is a polytropic process,

- The temperature variation in each chamber is negligible with respect to the supply temperature (so, we will consider $T_P = T_N = T$),

- The mass flow rate leakages are negligible, and

- The supply and exhaust pressures are constant.

2.3.1 Pneumatic Chambers

The pressure dynamics of the two chambers of the actuator can be approximated [13] as

$$\dot{P}_P = \frac{k}{V_P}(rT_PQ_P - A_PP_P\dot{y})$$

$$\dot{P}_N = \frac{k}{V_N}(rT_NQ_N + A_NP_N\dot{y}) \tag{2.9}$$

where P_P and P_N refer to pressures (Pa) inside the chambers P and N, respectively; Q_P and Q_N refer to mass flow rates (kg/s) of the chambers P and N, respectively; A_P and A_N refer to the piston cylinder areas (m²) in the chambers P and N, respectively; T_N and T_P refer to the temperature (K) in chambers N and P, respectively; k refers to the polytropic constant, r refers to the universal gas constant (J/(kgK)), and y refers to the piston position (m) shown in Figure 1.1. Note the arrows for position y and force τ_{Ext} and τ_{st} in Figure 1.1 refer to their positive directions. In addition, V_P and V_N refer to volumes (m³) of the chambers P and N, respectively, as shown below:

$$V_P = A_P(l/2 + y) \qquad V_N = A_N(l/2 - y) \tag{2.10}$$

where l is the total length of the chamber.

2.3.2 Valves

The mass flow rates Q_P and Q_N can be derived in terms of the discrete voltage inputs U_1, U_2, U_3, and U_4 shown in Figure 1.1 and the continuous pressure inputs P_P and P_N. Note that $U_i \in \{0,1\}$ where 0 refers to closed and 1 refers to open.

$$Q_P = U_1Q(P_S, P_P) - U_2Q(P_P, P_E) \tag{2.11a}$$

$$Q_N = U_3Q(P_S, P_N) - U_4Q(P_N, P_E) \tag{2.11b}$$

Here, P_S and P_E are the pressures of the compressed air supply and the exhaust/atmosphere respectively.

In general, $Q(P_{Up}, P_{Down})$ used in (2.11a) and (2.11b) in which P_{Up} is the upstream pressure and P_{Down} is the downstream pressure, refers to the expression for the mass flow rate through an orifice. As shown below, the model for the mass flow rate has two parameters: the critical pressure ratio b_{crit} and the mass flow rate constant $C_{val} = C\rho_0$ where C is the sonic conductance (m³/(s Pa)) and ρ_0 is the density of air (kg/m³) at a reference condition $T_0 = 293$K [3].

$$Q(P_{Up}, P_{Down}) = \begin{cases} C_{val}P_{Up}\sqrt{\frac{T_{Atm}}{T_{Up}}}\sqrt{1 - \left(\frac{\frac{P_{Down}}{P_{Up}} - b_{crit}}{1 - b_{crit}}\right)^2} & \text{, if } \frac{P_{Down}}{P_{Up}} > b_{crit} \text{ (subsonic)} \\ C_{val}P_{Up}\sqrt{\frac{T_{Atm}}{T_{Up}}} & \text{, if } \frac{P_{Down}}{P_{Up}} \leq b_{crit} \text{ (choked)} \end{cases} \tag{2.12}$$

Here, b_{crit} is the critical pressure ratio. The value $b_{crit} = 0.433$ comes directly from the data sheet of our solenoid valves, provided by Matrix-Bibus (BIBUS France S.A.S, Chaponnay, France). In the above, T_{Up} is the upstream temperature of air and T_{Atm} is the atmospheric temperature.

2.3.3 Piston

Finally, the dynamics of the mechanical actuator relating the applied force on the piston to the piston motion is

$$M\ddot{y} = (A_P P_P - A_N P_N) - b_V \dot{y} - \tau_{St} + \tau_{Ext} \tag{2.13}$$

where b_V is the viscosity coefficient (N s/m), M is the total mass of the load and the piston (Kg), τ_{St} is the stiction force (N), and τ_{Ext} is the external force (N). The stiction force τ_{St} was considered to be negligible since the pneumatic actuator used in our experiments was an Airpel anti-stiction cylinder (All Air Inc., New York, USA).

2.4 Discrete-Input Model of the Open-Loop Actuator

It is possible to combine the equations in Section 2.3 to write the dynamics of the open-loop pneumatic actuator in a 7-mode discrete-input form. Let us first find the overall dynamics of the system incorporating the dynamics of the pneumatic chambers, the valves, and the piston, which were reported in Section 2.3. Differentiating (2.13), solving for $\dddot{y}$, and substituting (2.9) and (2.10) in it, the dynamics of the actuator are obtained as the third-order equation

$$\dddot{y} = \frac{-b_V}{M}\ddot{y} - \frac{Ak}{M}\left(\frac{P_P}{l/2+y} + \frac{P_N}{l/2-y}\right)\dot{y} + \frac{krT}{M}\left(\frac{Q_P}{l/2+y} - \frac{Q_N}{l/2-y}\right) + \frac{\dot{\tau}_{Ext}}{M} \tag{2.14}$$

where l is the total length of the chamber.

As mentioned before, only one of the two valves U_3 and U_4 can be open at any given time to avoid a bypass of the chamber N. Similarly, only one of the two valves U_1 and U_2 can be open at any given time to avoid a bypass of the chamber P. From this, we find that there are a total of nine discrete modes for the solenoid valves [13]. These modes are shown in Table 2.1.

Reviewing these different discrete modes, we observe that the modes M_1, M_8, and M_9 are functionally similar (under no load) as they correspond to the two chambers being both closed, both venting, and both pressurized, respectively. For all of these three modes, the pressure difference across the chamber P and chamber N is reduced to zero over time. In fact, according to (2.13), the acceleration of the piston is influenced by the *difference* in pressures of the two chambers and, thus, from a functional perspective these three modes are the same under no load.

To reduce the controller design and tuning complexity, this thesis will focus on controllers that only utilize seven modes. The 7-mode modeling and control analysis and design in this thesis will concern the modes M_1 to M_7. M_1 was selected out of the three modes discussed above (M_1, M_8, and M_9) because it shows the highest resistance to piston motion which will improve the position tracking performance while under a load.

Table 2.1: Nine discrete modes of the open-loop actuator.

	M_1	M_2	M_3	M_4	M_5	M_6	M_7	M_8	M_9
U_1	0	1	0	0	0	1	0	0	1
U_2	0	0	1	0	0	0	1	1	0
U_3	0	0	0	0	1	0	1	0	1
U_4	0	0	0	1	0	1	0	1	0

From a functional perspective, we can describe the seven different operating modes listed in Table 2.1. In the operating mode M_1, both chambers are closed, as a result it has no active influence (i.e., actuation) on the system. In the operating mode M_2, chamber N is closed and chamber P is pressurized, thus the piston moves to the right. In the operating mode M_3, chamber N is closed and chamber P is exhausted, thus the piston moves to the left. In the operating mode M_4, chamber P is closed and chamber N is exhausted, again moving the piston to the right. In the operating mode M_5, chamber P is closed and chamber N is pressurized, again moving the piston to the left.

Worthy of note is that, in the operating modes M_2 to M_5, *one chamber is closed* while the other is pressurized or exhausted, making the piston actuation modest. However, in the operating mode M_6, chamber P is pressurized and chamber N is exhausted, moving the piston *as forcefully as possible* to the right. Similarly, in the operating mode M_7, chamber P is exhausted and chamber N is pressurized, moving the piston *as forcefully as possible* to the left.

For the seven discrete modes, the open-loop system dynamics can be obtained by substituting (2.11a) and (2.11b) into (2.14). We obtain

$$\ddot{y} = \begin{cases} f + \frac{\dot{\tau}_{Ext}}{M} & \text{, mode } M_1 \\ f + (-1)^i g_i + \frac{\dot{\tau}_{Ext}}{M} & \text{, mode } M_i, \ (2 \leq i \leq 7) \end{cases} \tag{2.15}$$

where i is an integer between 2 and 9 inclusively. In the above,

$$g_2 = \frac{krT}{M} \frac{Q(P_S, P_P)}{(l/2 + y)} \qquad g_3 = \frac{krT}{M} \frac{Q(P_P, P_E)}{(l/2 + y)}$$

$$g_4 = \frac{krT}{M} \frac{Q(P_N, P_E)}{(l/2 - y)} \qquad g_5 = \frac{krT}{M} \frac{Q(P_S, P_N)}{(l/2 - y)}$$

$$g_6 = g_2 + g_4 \qquad g_7 = g_5 + g_3$$

$$g_8 = g_4 - g_3 \qquad g_9 = g_5 - g_2$$

14

and

$$f = \frac{-b_V}{M}\ddot{y} - \frac{k}{M}\left(\frac{A_P P_P}{l/2 + y} + \frac{A_N P_N}{l/2 - y}\right)\dot{y} \tag{2.16}$$

Note that because $P_E \leq P_P \leq P_S$, $P_E \leq P_N \leq P_S$, $-l/2 \leq y \leq l/2$, and mass flow rates are non-negative functions, we have that g_2 through g_7 are all greater than or equal to zero. Also, g_8 and g_9 are close to zero and can be positive or negative.

Chapter 3

Sliding-Mode Control of A Single Pneumatic Actuator

3.1 Introduction

In this chapter[1], we consider a single pneumatic actuator comprised of two chambers as shown in Figure 1.1. Each chamber has two solenoid valves, each of which can be either closed, connected to a compressed air supply (source pressure), or connected to exhaust (atmosphere pressure). Having assumed the three modes in which both chambers are closed, both chambers are venting, and both chambers are pressurizing are functionally equivalent, then the system has a total of seven unique discrete modes. In this chapter, a sliding-mode controller forces the open-loop system to transition between these discrete operating modes, which were defined directly from the state of the on/off solenoid valves, based on the current tracking error.

   The organization of this chapter is as follows: The chapter introduction is given in Section 3.1. The operation and design of the sliding controller are discussed in Section 3.2. The simulation study to verify the control laws is shown in Section 3.3. The experimental results are presented in Section 3.4 while Section 3.5 contains the concluding remarks.

3.2 Sliding-Mode Controller Design

The proposed controller reacts differently depending on which of the seven modes the open-loop system is operating in at any given time. For a position-controlled system, we can define the sliding surface as $s = 0$ where s is a third order switching function selected as:

$$s = \frac{\ddot{e}}{\omega^2} + \frac{2\xi\dot{e}}{\omega} + e \qquad (3.1)$$

where e is the position error $y - y_d$, y is the actual position, y_d is the desired position, and ξ and ω are constant and positive numbers. We use this function s from (3.1) and invoke

---

[1]A version of this chapter has been accepted for publication in Mechatronics (A Journal of IFAC). Another version of this chapter has been published in Proceedings of IEEE/RSJ International Conference on Intelligent Robots and Systems (IROS), San Francisco, California, USA, September, 2011.

the seven different modes of the open-loop system based on five different regions of the s function. These regions of s and the selected operating mode of the system are illustrated in Table 3.1 – we will see the meaning of the last column in the next subsection. Please note that the input voltages (i.e., control actions) for each mode are listed in Table 2.1. If we employ a pneumatic controller based on Table 3.1, for the lowest error $|s| < \epsilon$, we use the mode M_1 which has no active influence on the system. For the largest positive error $s > \beta$, we use the mode M_7, which exerts the highest active influence in the negative direction on the system. Conversely, for the largest negative error $s < -\beta$, we use the mode M_6, which has the highest active influence in the positive direction.

Table 3.1: Selection of the operating mode based on positioning error s.

Region	Discrete operating modes	Magnitude of $\dot{s}$ from (3.6)
$s > \beta$	M_7	Large negative
$\beta \geq s > \epsilon$	M_3 or M_5	Modest negative
$\epsilon \geq s > -\epsilon$	M_1	Minimal
$-\epsilon \geq s > -\beta$	M_2 or M_4	Modest positive
$-\beta \geq s$	M_6	Large positive

In the next three subsections, first we discuss how closed-loop stability is guaranteed if the sliding controller properly transitions the open-loop system between its discrete operating modes. Next, within the stabilizing sliding control framework, we establish a hierarchy for transition between admissible modes such that closed-loop performance is improved. Then, we provide guidelines on the choice of threshold values that decide the transitions between modes.

3.2.1 Stability

To be able to analyze stability, consider the Lyapunov function candidate

$$V_{lya} = \frac{1}{2}s^2 \tag{3.2}$$

V_{lya} is a positive-valued function, therefore, if $\dot{V}_{lya} < 0$, V_{lya} will be decreasing. If V_{lya} is decreasing, $|s|$ will also be decreasing. Assuming s is initially bounded and $|s|$ is always decreasing, then s will always be bounded. Here, s will approach zero if we control the system so that

$$\dot{V}_{lya} = \dot{s}s < -\eta|s| \tag{3.3}$$

for some constant $\eta > 0$ [36][37][18]. This condition can be rewritten as

$$\begin{cases} \dot{s} > \eta & \text{if } s < 0 \\ \dot{s} < -\eta & \text{if } s > 0 \end{cases} \tag{3.4}$$

Take the derivative of (3.1) to get

$$
\begin{aligned}
\dot{s} &= \frac{\ddot{e}}{\omega^2} + \frac{2\xi\ddot{e}}{\omega} + \dot{e} \\
&= \frac{\dddot{y} - \dddot{y}_d}{\omega^2} + \frac{2\xi\ddot{e}}{\omega} + \dot{e}
\end{aligned}
\tag{3.5}
$$

By substituting (2.15) into (3.5) and assuming $\tau_{Ext} = 0$ we obtain

$$
\dot{s} = \begin{cases} \lambda & , \text{ mode } M_1 \\ \lambda + (-1)^i g_i / \omega^2 & , \text{ mode } M_i, \ (2 \le i \le 7) \end{cases}
\tag{3.6}
$$

where $\lambda = (f - \dddot{y}_d)/\omega^2 + 2\xi\ddot{e}/\omega + \dot{e}$. The function λ will be bounded if $\dot{y}$, $\ddot{y}$, $\dot{y}_d$, $\ddot{y}_d$, $\dddot{y}_d$, P_P, and P_N are bounded. The chamber pressures P_P and P_N are bounded between P_S and P_E. The desired position y_d is a controlled input to the system, thus y_d, $\dot{y}_d$, $\ddot{y}_d$, and $\dddot{y}_d$ are assumed to be bounded. If we rewrite (2.13) as

$$
M\ddot{y} + b_V \dot{y} = (A_P P_P - A_N P_N)
\tag{3.7}
$$

we see that the right side of (3.7) is always bounded. Therefore, (3.7) is a 1st order differential equation in terms of the velocity $(\dot{y})$, which means velocity is decaying exponentially if M and b_V are positive. Therefore, if $\dot{y}$ is initially bounded, then $\dot{y}$ will always be bounded. If we rewrite (2.13)

$$
\ddot{y} = \frac{1}{M}((A_P P_P - A_N P_N) - b_V \dot{y})
\tag{3.8}
$$

we find that it is defined purely in terms of bounded functions, thus it too must always be bounded and hence, λ is also bounded. Therefore, if the positive-valued functions g_2, g_4, and g_6 are sufficiently large, then modes M_2, M_4, and M_6 can ensure $\dot{s} > \eta$; this is appropriate when s is negative. Conversely, if the positive-valued functions g_3, g_5, and g_7 are sufficiently large, then modes M_3, M_5, and M_7 can ensure $\dot{s} < -\eta$; this is appropriate when s is positive. These two cases will be used to design a control strategy that satisfies (3.3).

All six functions g_2 to g_7 are linearly proportional to C_{val}, the valve's mass flow rate constant in (2.12), thus choosing a large enough valve will ensure that these scalar functions will be sufficiently large. Thus, using the modes M_2, M_4, or M_6 when $s < 0$, and using M_3, M_5, or M_7 when $s > 0$ will ensure (3.3), and thus the convergence to the sliding surface $s = 0$ over time. If s converges to zero and y_d, $\dot{y}_d$, and $\ddot{y}_d$ are bounded the output y, $\dot{y}$, and $\ddot{y}$ will also be bounded and thus the system will be BIBO stable.

3.2.2 Mode Selection

The 7-mode controller requires knowledge of the current chamber pressures as well as the current piston position to pick the appropriate operating modes. This requires additional sensors as compared to the 3-mode controller. For the case where we are trying to regulate

to a stationary y_d, we can use this additional mode data to minimize the switching required to bring y to y_d.

While there are unique control choices when $|s| > \beta$ or $|s| < \epsilon$, we require conditions for deciding which control mode to use when $\beta \geq |s| > \epsilon$ (see Table 3.1). For the positive region and the negative region there are two control modes: (M_5 and M_3) and (M_2 and M_4), respectively.

We will first study the negative region $-\beta \geq s > -\epsilon$. For the operating mode M_2, the chamber P is pressurized and chamber N is closed causing a moderate positive acceleration. If we evaluate (2.13) under mode M_2 and assume that the filling chamber has a sufficient amount of time to be fully pressurized we can see that the $\ddot{y} \propto (P_S - P_N)$. For operating mode M_4, the chamber N is being exhausted and chamber P is closed, also causing a moderate positive acceleration. If we evaluate (2.13) under mode M_4 and assume that the venting chamber has a sufficient amount of time to be fully vented we can see that the $\ddot{y} \propto (P_P - P_E)$. If we define

$$
\begin{aligned}
E_1 &= (P_S - P_N) - (P_P - P_E) \\
&= (P_S + P_E) - (P_P + P_N)
\end{aligned}
\tag{3.9}
$$

the magnitude of E_1 is positive when the pressure difference $P_S - P_N$ is greater than the pressure difference $P_P - P_E$. Therefore, when E_1 is positive, the appropriate operating mode for the region $-\epsilon \geq s > -\beta$ is M_2 as it will result in a higher piston acceleration compared to the mode M_4. Conversely when the magnitude of E_1 is negative M_4 will result in a higher piston acceleration compared to M_2.

In the positive region $\beta \geq s > \epsilon$, comparing modes M_5 and M_3, from (2.13) we see that the magnitudes of $\ddot{y}$ are based on the pressure differences $P_S - P_P$ and $P_N - P_E$ respectively. Let us define

$$
\begin{aligned}
E_2 &= (P_S - P_P) - (P_N - P_E) \\
&= (P_S + P_E) - (P_P + P_N) = E_1
\end{aligned}
\tag{3.10}
$$

the magnitude of E_2 is positive when the pressure difference $P_S - P_P$ is greater then the pressure difference $P_N - P_E$. Therefore, when E_2 is positive the appropriate operating mode for the region $\epsilon \geq s > \beta$ is M_5 as it will accelerate the piston more compared to mode M_3. Conversely when the magnitude of E_2 is negative mode M_3 will result in a higher piston acceleration compared to M_5. In summary, the magnitude of s in (3.1) and the magnitude of E_1 in (3.9) can be used by the controller to select the best of the seven operating modes see Figure 3.1.

3.2.3 Selecting Parameters τ, β, and ϵ

This section proposes appropriate methods for selecting the controller parameters of τ, β, and ϵ for the smoothest motions possible and the least switching activity. For these

parameters, the criterion for threshold selection was not unique. We chose the β and τ parameters based primarily on the velocity error. Refer to Table 3.3 for a summary of tuning parameters.

Selecting τ

The purpose of the timeout parameter τ is to reduce the switching between the modes used in the region $\beta \geq |s| > \epsilon$ by enforcing a minimum amount of time between mode transitions: M_5 to M_3, M_3 to M_5, M_2 to M_4, and M_4 to M_2. A larger τ value will reduce switching, by limiting the number of transitions. If the τ value is reduced; switching will increase, but the velocity output of the system will be a more consistent output; this will result in improved tracking performance. This is a performance trade-off; therefore, an appropriate value of τ should be determined by evaluating the open-loop responses M_2 and M_4.

For initial conditions (at $t = 0$) of $y = 0$ and $V_P = V_N = A\frac{l}{2}$ where $A = A_P = A_N$ (i.e., the piston positioned is halfway along the cylinder length), using (2.9) - (2.13) we can simulate the open-loop system response in each of these modes (Figure 3.2). These initial conditions were selected because they are symmetric in nature, and as such the modes M_5 and M_3 will be symmetric to modes M_2 and M_4. For the pressurizing case M_2 the initial conditions $P_P = P_N = P_E$ were selected. For the venting case M_4 the initial conditions $P_P = P_N = P_S$ were selected.

Evaluating the consistency of the output velocity of these two modes in Figure 3.2(a), we see that there is not a large variation in terms of the output velocity of each mode between 20 ms and 40 ms. As the switching activity is inversely related to the timeout value, we select the higher value of $\tau = 40$ ms to minimize switching. Thus, a minor change in the timeout τ will have a minimal impact in terms of tracking performance.

Selecting β

The magnitude β is the transition threshold between a mode connecting the two chambers to supply and exhaust pressures (i.e., M_6 or M_7), and the alternating modes for opening only a single valve (i.e., M_2/M_4 or M_3/M_5). To improve our understanding of this, we will evaluate the steady states of two different operating regions (from Table 3.1) : the region $s \leq -\beta$ (i.e., mode M_6) and the region $-\epsilon \geq s > -\beta$ (i.e., modes M_2 and M_4 alternating). Observe the open-loop responses of M_6 and M_2/M_4 in Figure 3.3. These open-loop responses were generated using the same initial conditions as seen in the previous sections pressurizing case. As it can be seen from Figure 3.3 the velocity of the piston increases to a maximum. If we approximate the nominal velocity in each region to be half of its maximum velocity, we can select the mode transition threshold between the two regions as the average of the region's nominal velocities.

To approximate the maximum piston velocity we select the following conditions to maximize the velocity: $\ddot{y} = 0$, $F_{St} = 0$, $P_P = P_S$, $P_N = P_E$, $A_P = A_N = A$, and $F_{Ext} = 0$.
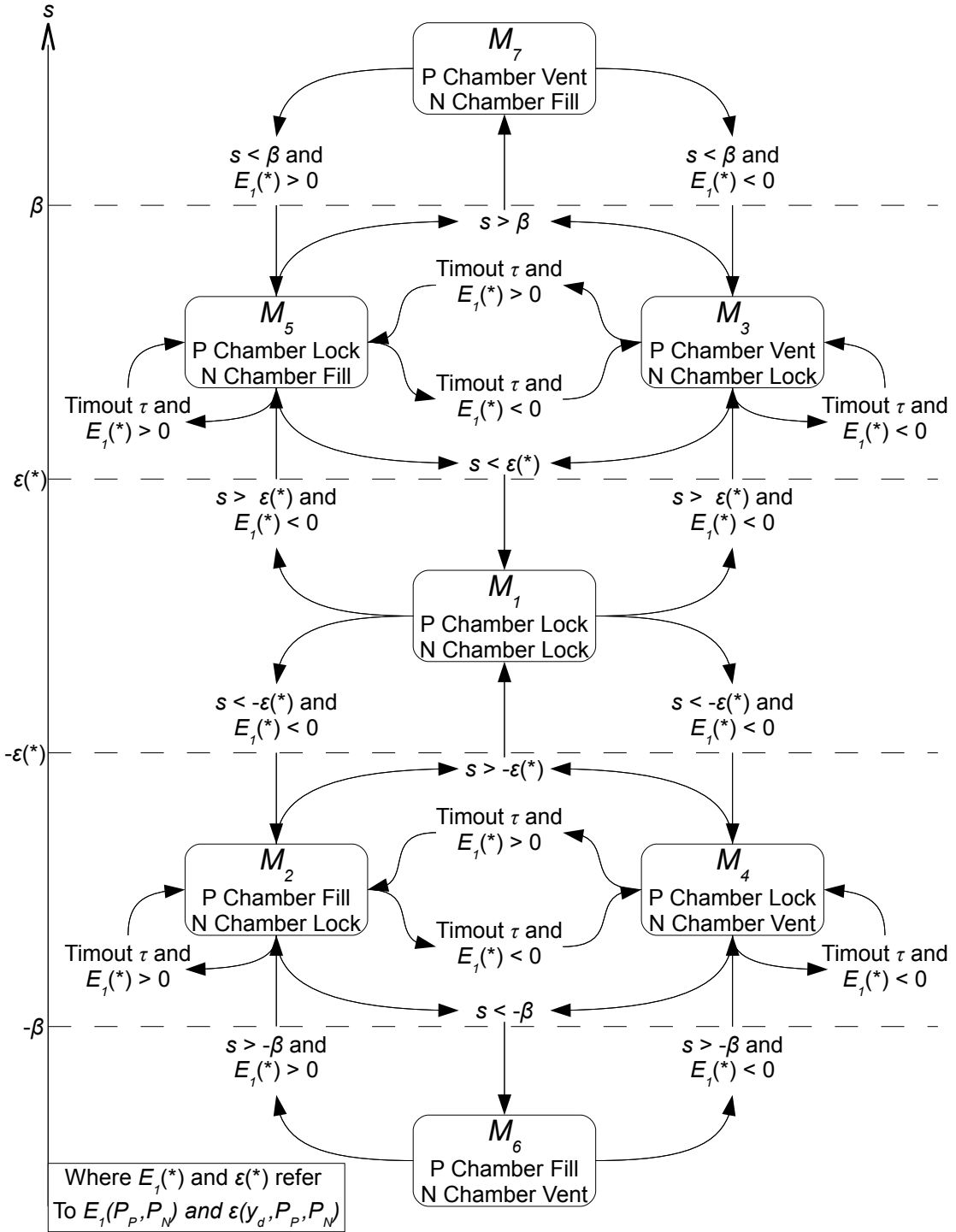
Figure 3.1: 7-mode controller diagram.
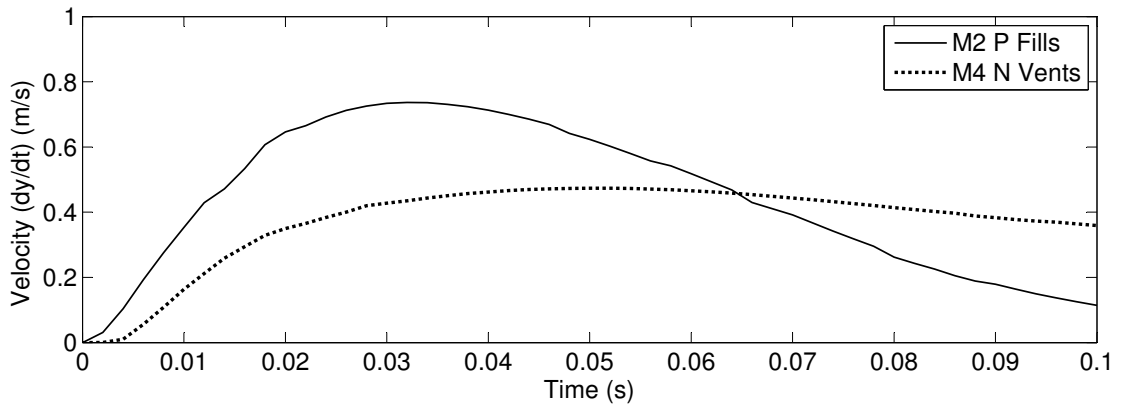
(a) Piston Velocity (m/s)
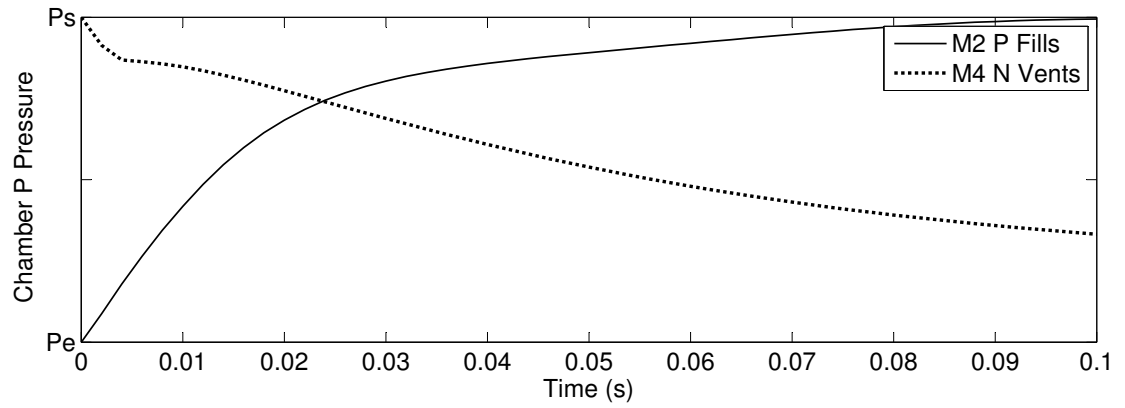
(b) Chamber P Pressure
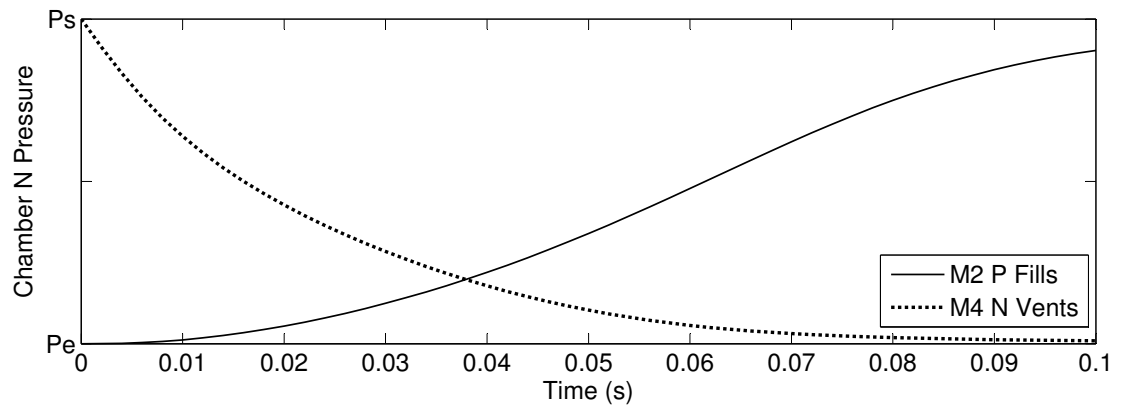
(c) Chamber N Pressure

Figure 3.2: Open-loop responses of modes M_2 and M_4.
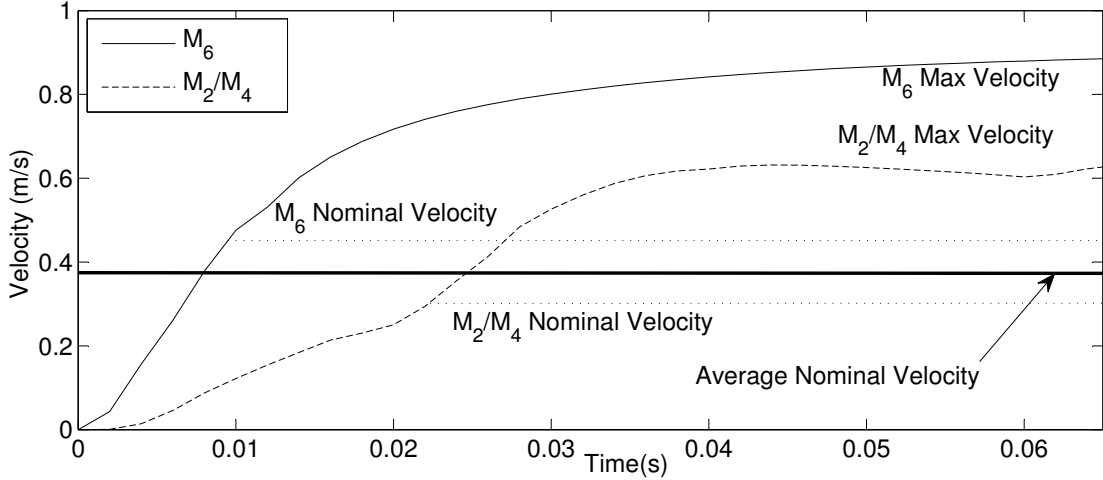
Figure 3.3: Open-loop responses of modes M_6 and M_2/M_4.

Substituting these conditions into (2.13) we find the maximal velocity as

$$\max(\dot{y}) = \frac{A(P_S - P_E)}{b_V} \tag{3.11}$$

From a time-averaged perspective, the M_2/M_4 modes have approximately half the air flow (of the M_6 mode) since only half the orifices are open at any given time. Therefore, the M_2/M_4 modes' maximum velocity can be approximated as half of $max(\dot{y})$. From this, the nominal velocity of each region can be approximated as $\frac{1}{2}max(\dot{y})$ and $\frac{1}{4}max(\dot{y})$, making the transition threshold equal to $\frac{1}{2}(\frac{1}{2}max(\dot{y}) + \frac{1}{4}max(\dot{y})) = \frac{3}{8}max(\dot{y})$. In terms of β we multiply the threshold by $\frac{2\xi}{\omega}$ to convert this transition point into the function s in (3.1) to get:

$$\beta = \frac{3\xi}{4\omega}\max(\dot{y}) = \frac{3\xi A(P_S - P_E)}{4b_V\omega} \tag{3.12}$$

This selection of β is not unique; however it has been demonstrated in simulation results as being appropriate.

Selecting ϵ

When the magnitude of s is less than a positive-valued but small ϵ, the controller removes the actuation from the system by closing all valves. The magnitude of ϵ should ideally be selected so that when this occurs and the effect of past actuations settles out, the position difference, $y - y_d$, will be less than some desired small amount e_{min}. Here, e_{min} is an appropriate value for ϵ for tracking a non-stationary desired position ($\dot{y}_d \neq 0$). However, when the system is moving towards a stationary desired position ($\dot{y}_d = 0$) and the valves of the system are closed (for both chambers P and N), the piston does not immediately stop. When the valves are shut the pressure difference between chambers P and N will go to zero only after the final position has overshot past the desired position. Ideally, the system

23

should have shut all the valves before reaching the desired position so that the final settled position y would be close to y_d.

When the valves are shut, all flow rates are equal to zero (i.e., $Q_P = Q_N = 0$). For initial pressures P_N and P_P and final pressures P_{PF} and P_{NF}, the total molecules in each chamber will be the same. Thus, the initial pressure and final pressure can be equated as follows

Table 3.2: The ϵ transition table.

	Intial state	Final state
Pressure	$P_P \neq P_N$	P_{PF}, P_{NF}
Position	y	y_f
Velocity	$\dot{y} \neq 0$	$\dot{y}_f = 0$
Acceleration	$\ddot{y} \neq 0$	$\ddot{y}_f = 0$

$$PV = P_F V_F \tag{3.13}$$

based on the ideal gas law. From this, we find the following relationships between pressures and positions

$$P_{PF}A(\frac{l}{2} + y_f) = P_P A(\frac{l}{2} + y) \qquad P_{NF}A(\frac{l}{2} - y_f) = P_N A(\frac{l}{2} - y) \tag{3.14}$$

where y is the initial position and y_f is the final position. This equation assumes a k value of 1 to simplify the math. Therefore, the selection of the ϵ threshold is based on this simplification.

By evaluating (2.13) at the stationary point ($\ddot{y} = \dot{y} = 0$) and substituting (3.14), we obtain

$$(P_{PF} - P_{NF}) = 0$$

$$P_P \frac{\frac{l}{2} + y}{\frac{l}{2} + y_f} - P_N \frac{\frac{l}{2} - y}{\frac{l}{2} - y_f} = 0 \tag{3.15}$$

Solving for y and substituting y_d for the final position y_f, we find

$$y = \frac{P_N(y_d + \frac{l}{2})l}{P_N(y_d + \frac{l}{2}) + P_P(\frac{l}{2} - y_d)} - \frac{l}{2} \tag{3.16}$$

Solving for e we find

$$e = \frac{P_N y'_d l}{P_N y'_d + P_P(l - y'_d)} - y'_d \tag{3.17}$$

where $y'_d = y_d + \frac{l}{2}$.

Immediately after the system switches to mode M_1, the pistons' position y is approaching y_d and, therefore, e will be either a positive or negative value with a sign opposite the sign

of $\dot{y}$. Since the threshold ϵ is always a positive magnitude, we are interested in $|e|$. We convert this transition point into the function s in (3.1) to get:

$$s_{stop} = \left| \frac{P_N y_d' l}{P_N y_d' + P_P(l - y_d')} - y_d') \right| \tag{3.18}$$

To utilize this threshold in experiment two conditions must be met: The equation (3.18) requires $\dot{y}_d$ to be 0. And the velocity $\dot{y}$ must be travelling in a direction that approaches the sliding surface $s = 0$. We implement this control using the following function:

$$\epsilon = \begin{cases} \kappa_\epsilon s_{stop} & , (s\dot{e}) < 0 \text{ and} \\ & |\dot{y}_d| < \dot{y}_{d\_min} \\ e_{min} & , \text{ otherwise} \end{cases} \tag{3.19}$$

where $\dot{y}_{d\_min}$ was measured from the experimental setup. For a stationary actuator the measured velocity varied by ± 15 mm/s, therefore, $\dot{y}_{d\_min} = 20$ mm/s was selected. The theoretical value of κ_ϵ should be equal to 1, however experimentally it was found that the system required some additional resistance. Therefore, its value was increased to $\kappa_\epsilon = 2$.

With this equation, if $\dot{y}_d \neq 0$, then the system is actively tracking y_d. However, if $\dot{y}_d \approx 0$, then it will reduce switching activity by stopping at the point that will settle on y_d without over-shooting the target. The equations (3.18) and (3.19) which calculate ϵ require that the values of P_N, P_P, and y_d are measured.

Figure 3.4 shows the experimental results of testing the 7-mode controller with a fixed ϵ and a variable ϵ. The actuation is removed much sooner on the variable ϵ and as a result, coasts to a stop on the desired position with no further correction required. However, when the 'fixed ϵ' controller actuation is removed too late, it must immediately go in the reverse direction (mode 7) to try and reduce overshoot.

Table 3.3: Tuning parameters table.

Par.	Physical meaning	Effect on the performances	Tuning/ Selection method	Experimental/ Theoretical value
τ	Used when $\epsilon \geq |s| \geq \beta$, the minimum time between modes	Small τ increases switching and improves tracking performance	Calculated from simulation	40 ms/ 40 ms
e_{min}	The s threshold between actuation and no actuation	Large e_{min} reduces chattering and tracking precision	Desired tracking precision	1.0 mm/ 1.0 mm
β	The s threshold for using a higher drive potential	Small β strengthens piston actuation	(3.12) using an estimation of $\max(\dot{y})$	3.0 mm/ 3.7 mm
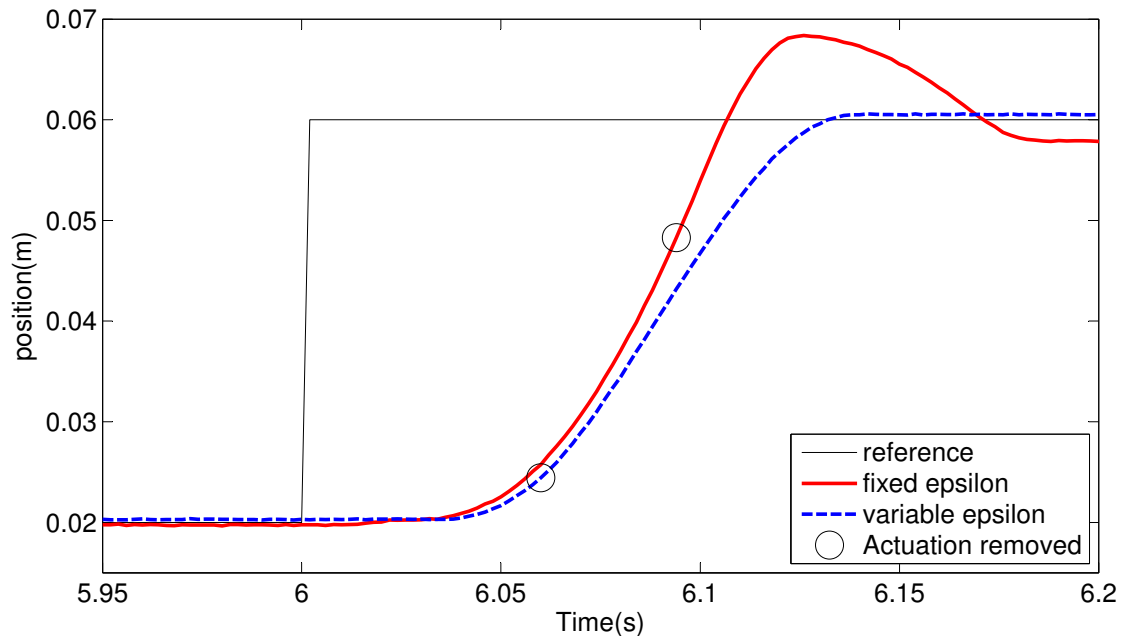
Figure 3.4: Experimental result of variable ϵ vs. fixed ϵ.

3.3   Simulation Study

To analyze the performance of the 7-mode controller described in this chapter we will be comparing it to the original 3-mode controller it was based on. The state diagram for the 3-mode controller is show in Figure 3.5. The e_{min} shown in Figure 3.5 is from (3.19).

3.3.1   Simulation Parameters and Test Inputs

For our simulation, we selected the model parameters listed in Table 3.4. These model parameters correspond to the experimental setup that will be used in Section 3.4.

Table 3.4: System parameters table.

Var.	Value	Label
l	0.1 m	Chamber Length
T	296 K	Chamber Temperature
C_{val}	3.4×10^{-9} kg/(s Pa)	Mass Flow Rate Const.
P_S	$300,000$ Pa	Supply Air Pressure
P_E	$100,000$ Pa	Exhaust Air Pressure
k	1.2	polytropic constant
A	1.814 cm^2	Piston Cylinder Area
b_V	50 (N s)/m	Viscosity Coefficient
M	0.9 kg	Total Mass of load

For the controller $e_{min} = 1$ mm. To model our system, we utilized the Simulink Simscape
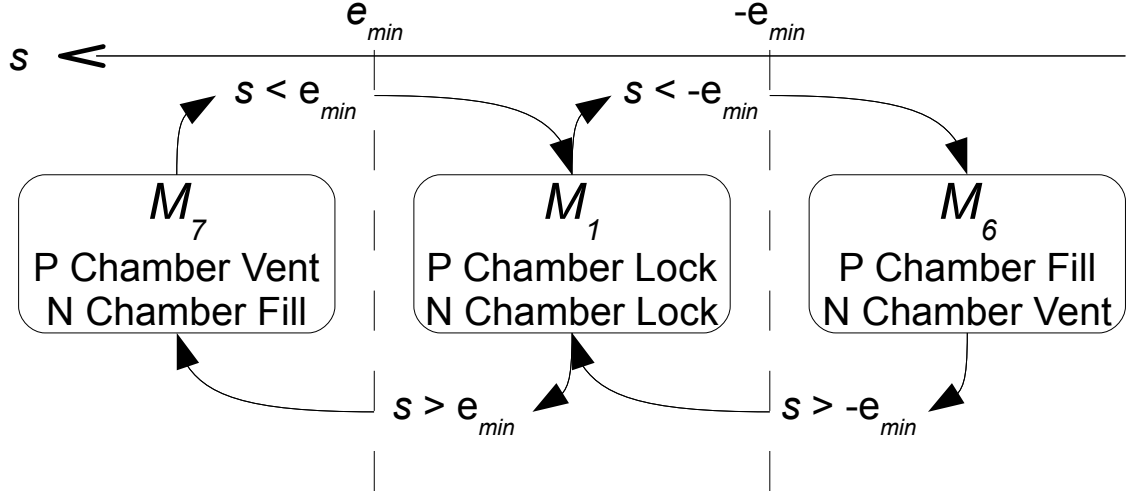
Figure 3.5: 3-mode state diagram.

toolbox in Matlab, which includes pneumatic elements.

There were a total of 3 different test inputs used:

1. Sine-wave:

$$y_d = 0.020 sin(2\pi ft) \tag{3.20}$$

2. Multi-sine wave:

$$y_d = \frac{0.030}{m} \sum_{i=1}^{m} sin(2\pi \frac{fi}{m}t) \quad m = 8 \tag{3.21}$$

3. Square-Wave:

$$y_d = \begin{cases} 0.020 & , |t| < T_{period}/2 \\ -0.020 & , T/2 \le |t| < T_{period} \end{cases} \tag{3.22}$$

Over a period of $T_{period} = 1/f$.

For our simulations, we selected $\omega = 100$ rad/s, $\xi = 0.5$, $\tau = 40$ ms, $\beta = 3.0$ mm, and $e_{min} = 1.0$ mm.

3.3.2   Simulation Results

The simulation was run utilizing the sine-wave test input with frequencies varying from 0.1 Hz - 3.0 Hz, the results of the simulations are charted in Figure 3.6(a). From these results, we find that for both the 3-mode and the 7-mode systems increasing the input frequency leads to an increase in RMS tracking. The inability of the systems to track y_d for higher frequency input sine-waves is due to a limitation of flow capability of the valves to drive the actuator at the higher velocities.

The advantage of the 7-mode controller algorithm is the reduction in the solenoid valves switching as observed in Figure 3.6(a). At 1.5 Hz, this is equal to 63% reduction in switching activity and a 0.45 mm improvement in tracking error.

Higher actuator velocities are required for high frequency sine waves. The dynamic friction of a pneumatic actuator limits the magnitude of the output velocity. As the desired velocity approaches the maximum actuator velocity, both the 3-mode and 7-mode tracking error converges due to saturation. For low frequency sine waves, lower actuator output is required. As the required actuator output decreases, both the 3-mode and 7-mode controllers start to control the actuator such that the actual output exceeds the required output and as a result position-overshoot increases the tracking error. In simulation the tracking error is shown in Figure 3.6(a) to converge at high and low frequencies.

To test the system with a more complicated signal, we used an input that is a summation of 8 sine-waves with 8 different frequencies. For this simulation we will use $f = 1$ Hz. As we can see from Figure 3.7(a), both controllers have no trouble tracking the multi-sine wave; however, the switching activity (demonstrated by the open/close motions of the two valves in the P chamber) for the 7-mode controller is greatly reduced compared to the 3-mode controller. From the 3-mode controller to the 7-mode controller, there is a 75% reduction in solenoid switching activity. To further test the controller, we utilized a square-wave function. The results of this testing can be observed in Figure 3.7(b). From the simulation, we find that the 3-mode controller has difficulty regulating at a fixed setpoint, which causes the switching to be on average 263.2 times per second. The 7-mode controller, however, minimizes the switches required to move between thresholds, resulting in a 76.6 switches per second on average. This switching per second count reflects the aggregated occurrence of switches in all 4 solenoid valves in each control modality.

The pneumatic system used in our experiments has solenoid valves that are switched at a rate of up to 500 Hz due to a valve switching time (response time) of 2 ms. In simulations, we have the flexibility to increase or decrease the valve switching time. To observe the effect of this, we have simulated a system with a 1.5 Hz sine-wave reference position and with the 3-mode and 7-mode controllers over a range of valve switching times varying from 0.1 ms to 10 ms. The results of these simulations have been plotted in Figure 3.6(b). It can be seen from these results that increasing the valve switching time increases the tracking error. It can also be seen from this plot that the switching activity for the 7-mode controller is always less than the 3-mode controller. The tracking error is also found to be consistently better for the 7-mode controller versus the 3-mode controller.

3.4   Experimental Testing

In this section, experiments with a 1-DOF system are reported. As illustrated in Figure 3.8, the setup consists of a pneumatic manipulator. The low friction cylinders (Airpel model M16D100D) have a 16 mm diameter and a 100 mm stroke. The piston is connected to a mass of approximately M = 900 g. The pneumatic solenoid valves (Matrix model GNK821213C3K) used to control the air flow have switching times of approximately 1.3 ms (opening time) and 0.2 ms (closing time). With such fast switching times, the on/off
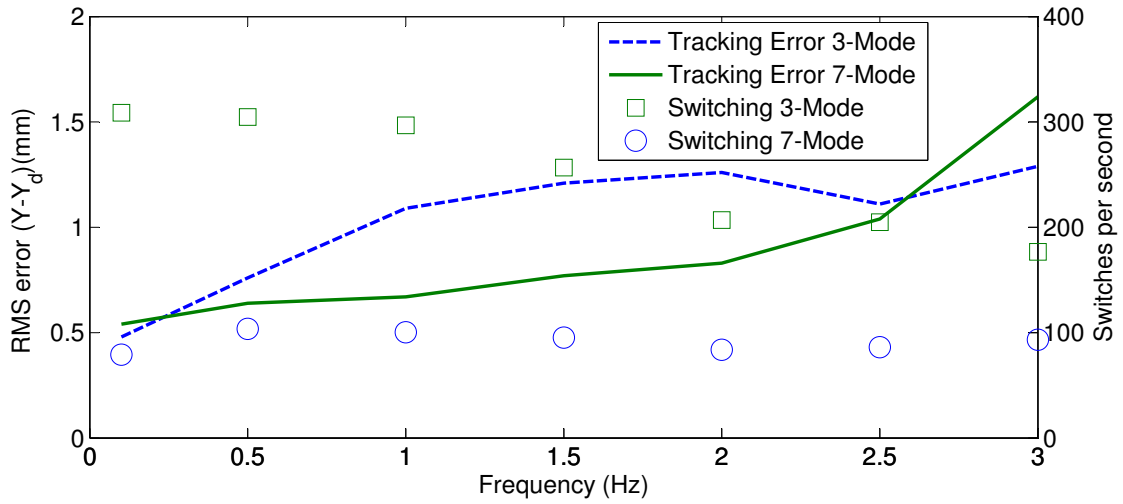
(a) Versus frequency.
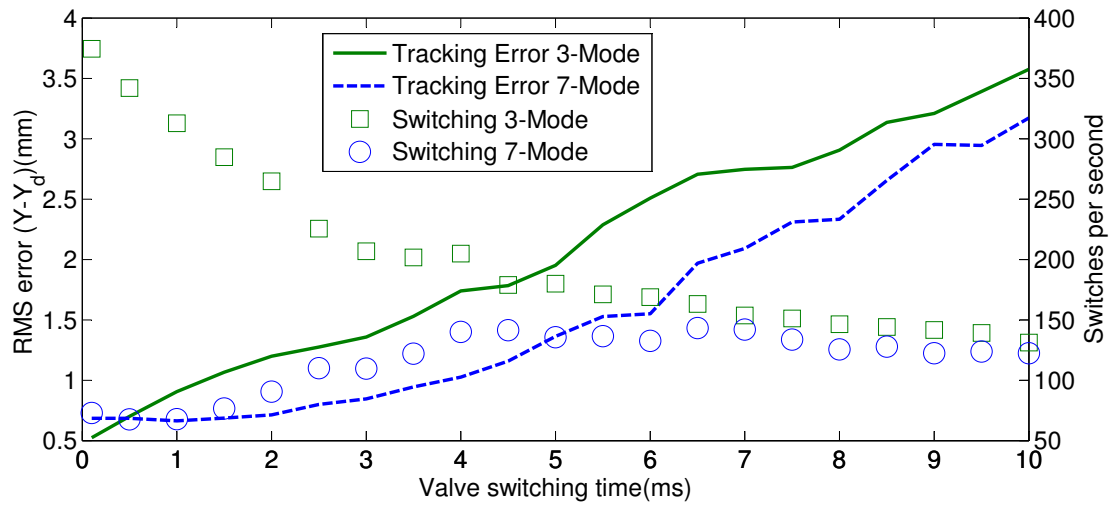
(b) For a 1.5 Hz sine-wave reference trajectory versus the valve response time.

Figure 3.6: Position tracking and switching activity simulation results for a sine-wave reference trajectory.
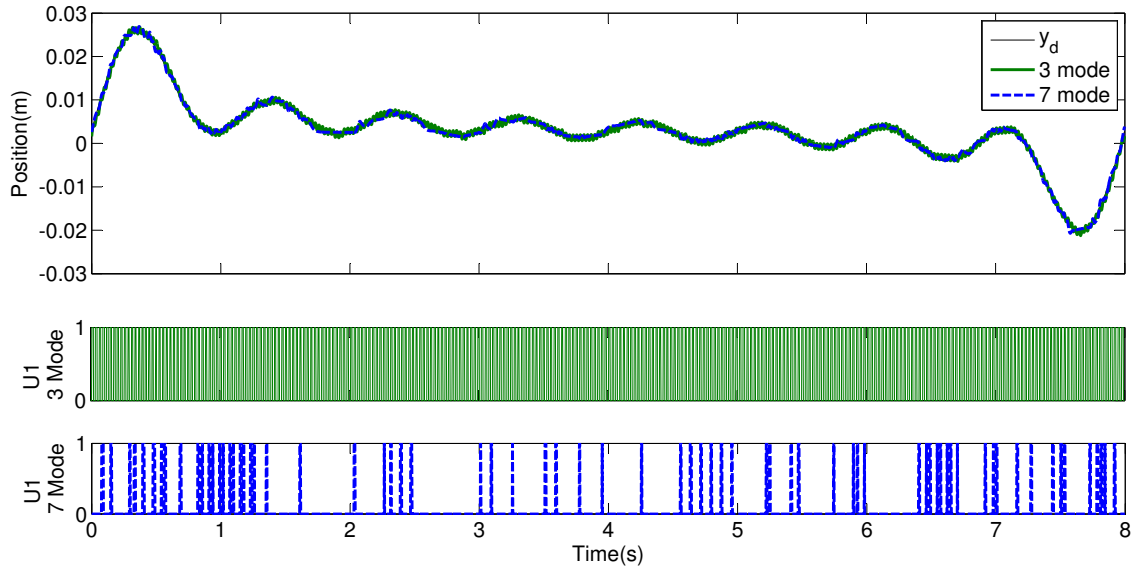
(a) For a multi-sine-wave reference trajectory.
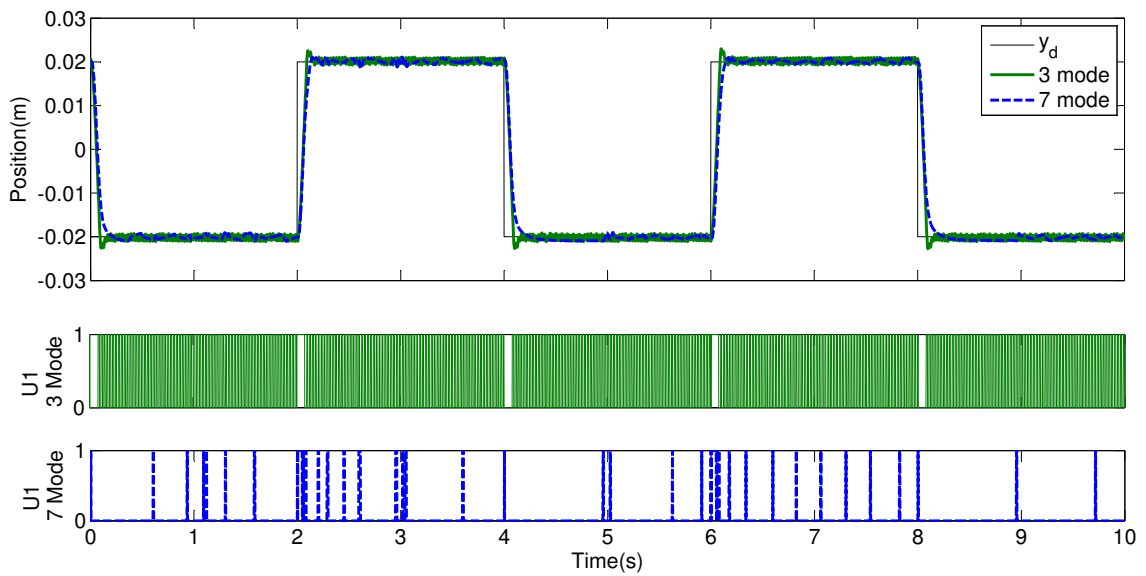
(b) For a square-wave reference trajectory.

Figure 3.7: Position tracking and switching activity simulation results.
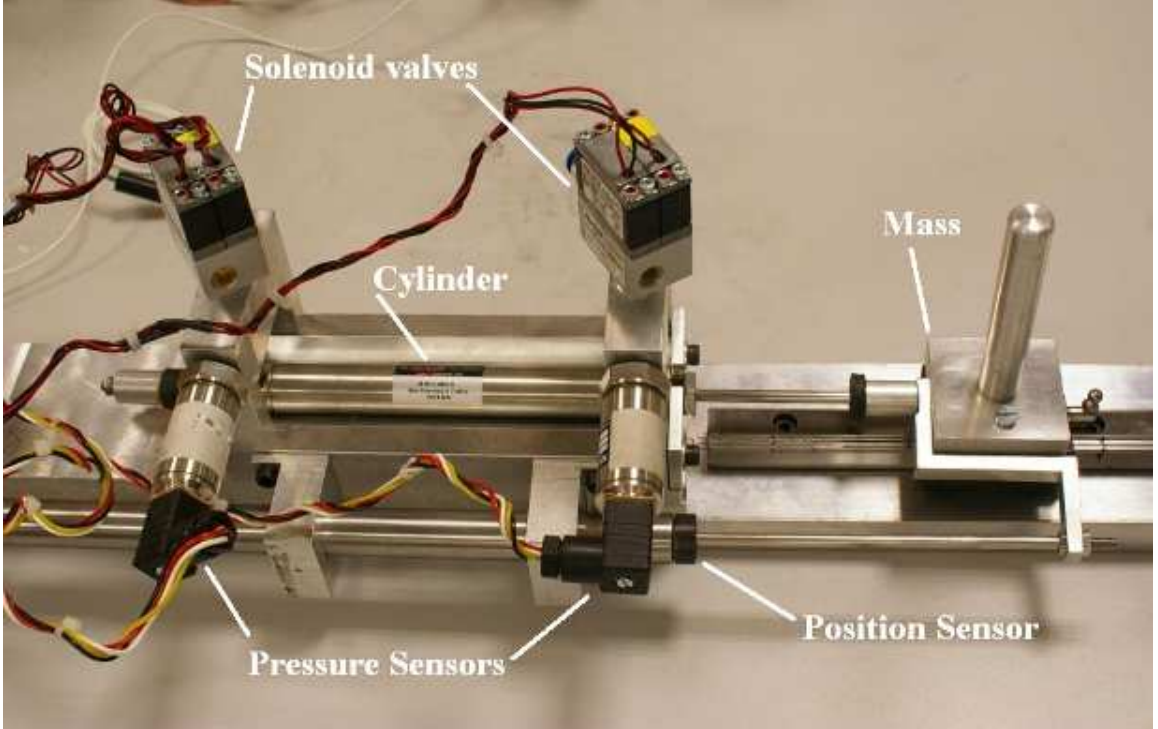
Figure 3.8: Experimental setup.

valves are appropriate for the purposes of the proposed controller. In terms of sensors, a low-friction linear variable differential transformer (LVDT) is connected to the cylinder in order to measure the linear positions.

The controller is implemented using a dSPACE board (DS1104), running at a sampling rate of 500 Hz. This value has been chosen according to the open/close bandwidth of the switching valves and to guarantee an acceptable tracking response. For this experiment, the following controller parameters were selected: $\omega = 60$ rad/s, $\xi = 0.5$, $\tau = 0.04$ s, $\beta = 3.0$ mm, and $e_{min} = 1.0$ mm. The parameters ω and ξ were selected based on the desired output dynamics; whereas, τ, β, and e_{min} were selected based on Table 3.3.

3.4.1 Experimental Switching Function

Our experimental setup has a position sensor, but does not have an accelerometer or velocity measurement. This section describes how the switching function s in (3.1) was obtained for experimental setups. The first derivative of the position error in (3.1) is computed through a backward difference method applied on the position signal followed by a de-noising second-order Butterworth filter with a cutoff frequency of 50 Hz. The second derivative is computed in the same way from the filtered first-derivative signal. The filter bandwidth was chosen to be large enough (50 Hz) with respect to the input's bandwidth of the system (less than 5 Hz).

The following finite difference equations were then used to find the first and second

31

derivatives.

$$\dot{e}_{filt}(j) = \frac{e_{filt}(j) - e_{filt}(j-1)}{T_{period}} \tag{3.23}$$

$$\ddot{e}_{filt}(j) = \frac{e_{filt}(j) - 2e_{filt}(j-1) + e_{filt}(j-2)}{T_{period}^2} \tag{3.24}$$

Where e_{filt} was the filtered tracking error. Substituting (3.23) and (3.24) into (3.1) produces

$$s_{exp} = \frac{\ddot{e}_{filt}}{\omega^2} + \frac{2\xi\dot{e}_{filt}}{\omega} + e_{filt} \tag{3.25}$$

3.4.2 Experimental Results

The experiment was run utilizing the sine-wave test input for the desired position, y_d, with frequencies varying from 0.1 Hz - 3.0 Hz. The recorded results from these experiments are charted in Figure 3.9(a). From these results, we find that for both the 3-mode and the 7-mode systems, increasing the input frequency increases the RMS tracking error (as shown in the simulated results). When we compare the results for the 3-mode controller and the 7-mode controller, we can see that there was a notable improvement in tracking performance for the 7-mode controller; as well as a notable decrease in switching activity in the 7-mode case (as was demonstrated before in the simulated results).

Next, the experiment was run utilizing a square-wave test input for the desired position, y_d. The recorded results from these experiments are charted in Figure 3.10(b). From these results, we find that for the 3-mode case there is an 18% positive overshoot in the position tracking. For the 7-mode case the positive overshoot obtained was only 1.9%. This is the due to the variable ϵ threshold applied to the 7-mode controller removing actuation sooner; allowing the actuator to coast to a stop at the y_d position. This results in improved tracking performance and reduced switching activity.

To test the system with a more complicated signal, we used an input that is a summation of 8 sine-waves with 8 different frequencies.

For this simulation we will use $f = 1$ Hz. As we can see from Figure 3.10(a), both controllers have no trouble tracking the multi-sine wave; however, the switching activity (demonstrated by the open/close motions of the two valves in the P chamber) for the 7-mode controller is reduced compared to the 3-mode controller as was seen in simulation. From the 3-mode controller to the 7-mode controller, there is a 48% reduction in solenoid switching activity.

To test the system's ability to reject external force disturbance, the experiment was run again utilizing the sine-wave test input with a weight attached to the actuator via a cord and pulley. The weights tested were 0.5 kg (see Figure 3.9(b)) and 1.0 kg (see Figure 3.9(c)). These weights applied a constant force that was approximately equal to gravity in the positive direction of the actuator. To prevent the weights attached to the actuator from swinging like a pendulum only frequencies from 0.1 Hz - 1.5 Hz were utilized. Tracking
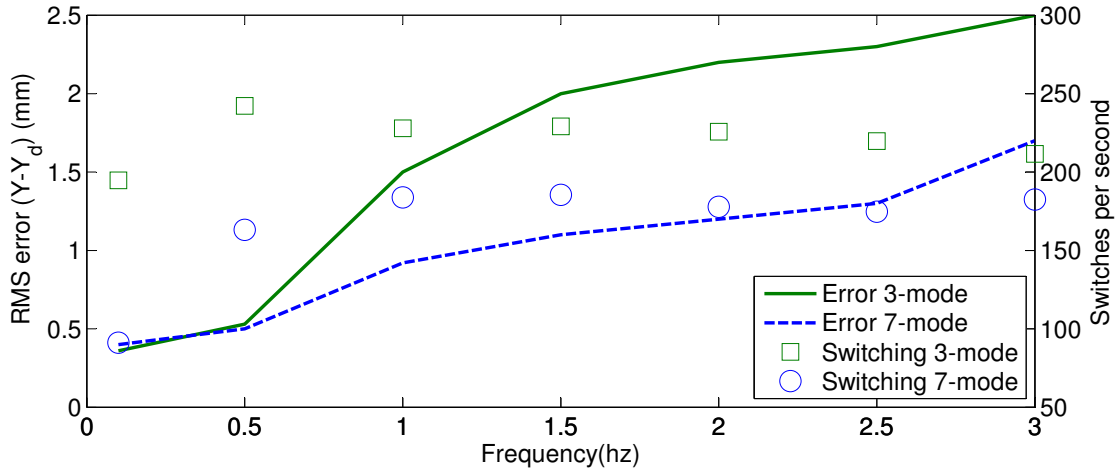
(a) No Load on Pulley
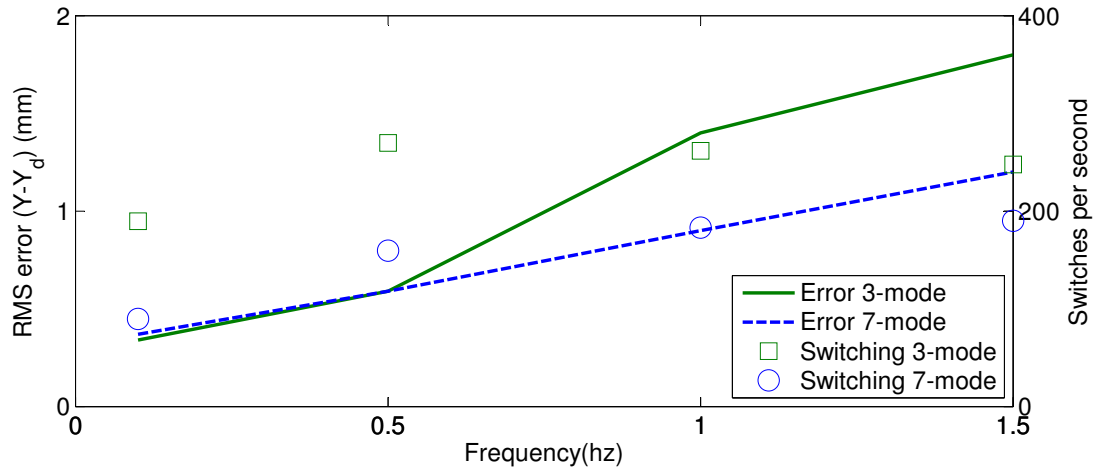
(b) 0.5 kg Load on Pulley
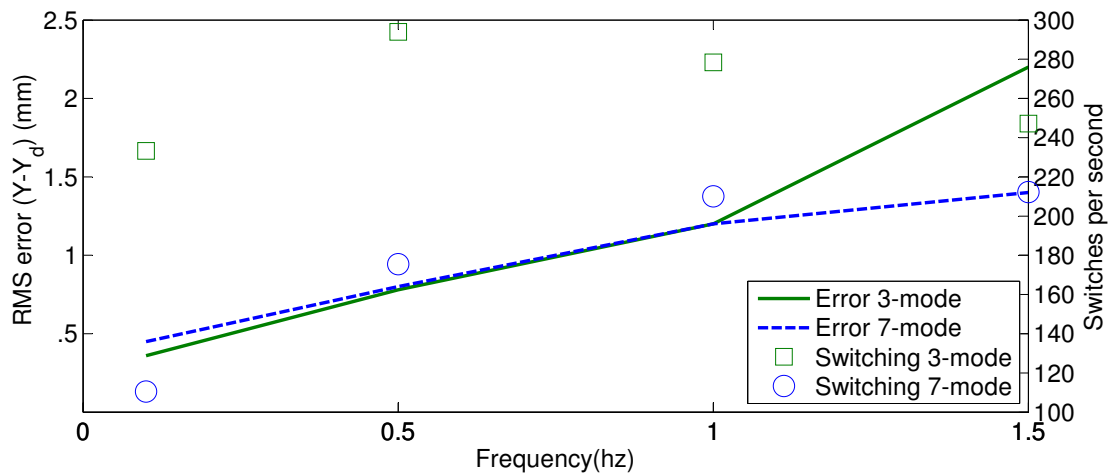
(c) 1.0 kg Load on Pulley

Figure 3.9: Position tracking and switching activity experimental results for a sine-wave reference trajectory.
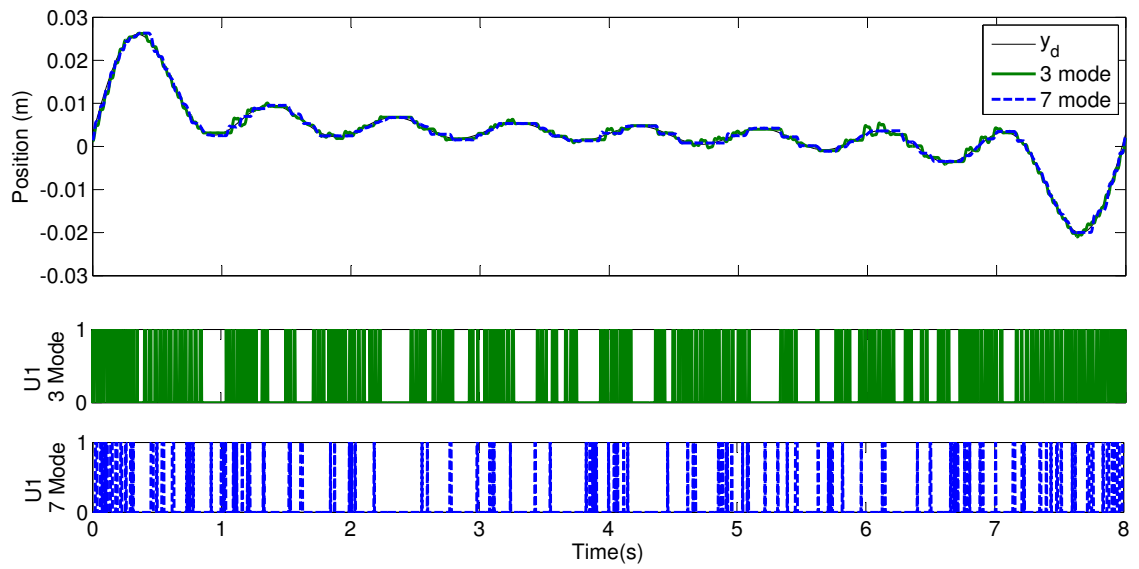
(a) For a multi-sine-wave reference trajectory
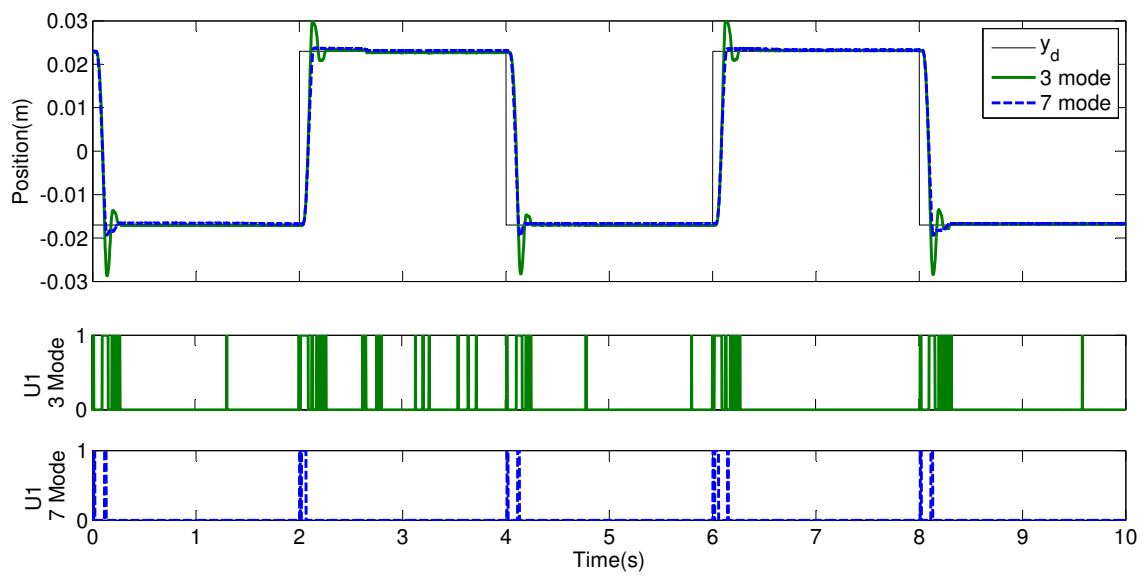
(b) For a square-wave reference trajectory

Figure 3.10: Position tracking and switching activity experimental results.

error was not significantly increased as a result of attaching the weights; valve switching activity was marginally increased.

The first objective of the simulation study was to validate the feasibility of the proposed control scheme before implementing it on the physical system. As in any other design, the simulation study helped to obtain an idea of the controller gains to be used in the experiments. Interestingly, while the simulated model was somewhat different from the experimental system, the good experimental results show the robustness of the proposed controller against unmodelled temperature dynamics and model parameter uncertainties.

3.5   Concluding Remarks

This chapter proposed a sliding-mode law for precise position control with minimal switching activity designed for use on a pneumatic actuator. This controller uses four additional modes as compared to [18], which decrease the coarseness in the drive force resulting in lower position tracking errors and reducing the open/close activity of the valves which increases the valves' lifespan.

In order to experimentally evaluate the proposed control strategy, a comparison study has been performed relative to the 3-mode controller of [18] for a position tracking problem. The results show that the tracking accuracy is better in the case of 7-mode control than in the 3-mode control. Also, the 7-mode controller was shown to lead to a significant reduction in the switching of the solenoid valves compared to the 3-mode control. This implies that the valve's lifetime will be longer and the overall reliability of the components will be better when the proposed control law is utilized.

Chapter 4

Sliding-Mode Control of A Teleoperator with Two Pneumatic Actuators

4.1   Introduction

In Chapter 3, a sliding-mode control scheme was developed that extended the three-mode control to seven-mode control. It was demonstrated that for a single pneumatic actuator, expanding the control possibilities from three-mode control to seven-mode control reduced the tracking error and the valves' switching activity, causing an overall improvement in the system performance. This is due to the fact that the four additional modes of operation help to utilize only the necessary amounts of drive energy allowing smoother control of the nonlinear system.

In this chapter, we extend the application of the seven-mode controller from the position control of a single robot to the bilateral control of a telerobot. We will show that this results in reduced position tracking error and solenoid valve switching activity for the teleoperation system. The proposed sliding-mode control schemes are experimentally validated on a pair of actuators connected under the position-position and the force-position teleoperation architectures. We will be showing that leveraging the additional modes of operation leads to a smoother control of the teleoperated actuator.

The organization of this chapter is as follows: The chapter introduction is in Section 4.1. A sliding-mode control of a teleoperated pair of solenoid-valve actuators is reported in Section 4.2. The experimental results are shown in Section 4.3. The analysis of the results is shown in Section 4.4. Finally, the concluding remarks are presented in Section 4.5.

Table 4.1: Master/slave actuator variable names where $q \in \{P, N\}$, $v \in \{1, \ldots, 7\}$, and $t \in \{1, \ldots, 7\}$.

Single robot	y	P_q	V_q	τ_{Ext}	g_t	f
Master	y_m	$P_{q,m}$	$V_{q,m}$	τ_h	$g_{v,m}$	f_m
Slave	y_s	$P_{q,s}$	$V_{q,s}$	$-\tau_e$	$g_{t,s}$	f_s
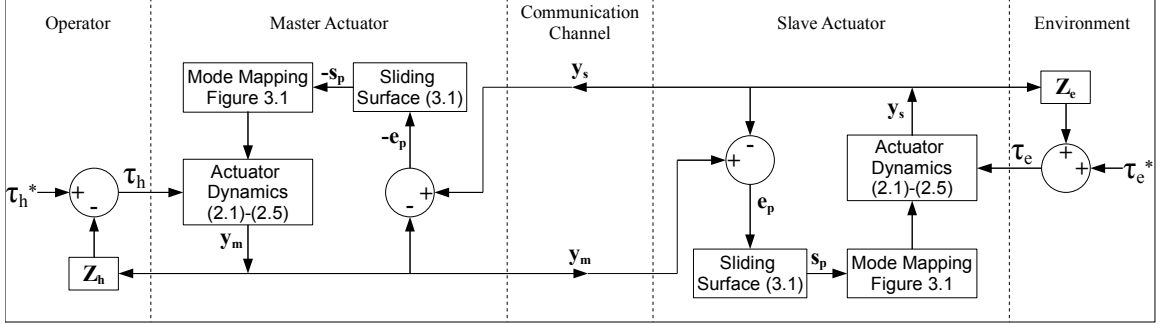
Figure 4.1: Position-position based teleoperation.

4.2 Sliding-Mode Control of a Teleoperator with Two Pneumatic Actuators

For the teleoperation system, we assume that the master and slave dynamics will be the same as those described in Section 2.3. For different actuators, the common variables will be re-labeled as shown in Table 4.1.

4.2.1 Position-Position Control

The block diagram in Figure 4.1 shows the architecture of the position-position based bilateral teleoperation system. In this setup, the human operator dynamics, Z_h, and the environment dynamics, Z_e, are unknown or uncertain. The nonlinear actuator dynamics are described in (2.9)-(2.13).

The equations for the master and slave dynamics are

$$M\ddot{y}_m = A(P_{P,m} - P_{N,m}) - b_V \dot{y}_m + \tau_h$$
$$M\ddot{y}_s = A(P_{P,s} - P_{N,s}) - b_V \dot{y}_s - \tau_e \tag{4.1}$$

Differentiating (4.1) and substituting (2.9) and (2.10) into it, the dynamics of the two systems are obtained as

$$\dddot{y}_m = \begin{cases} f_m + \dot{\tau}_h/M & , \text{mode } M_1 \\ f_m + (-1)^v g_{v,m} + \dot{\tau}_h/M & , \text{mode } M_v \neq M_1 \end{cases}$$

$$\dddot{y}_s = \begin{cases} f_s - \dot{\tau}_e/M & , \text{mode } M_1 \\ f_s + (-1)^t g_{t,s} - \dot{\tau}_e/M & , \text{mode } M_t \neq M_1 \end{cases} \tag{4.2}$$

37

where $v \in \{1, \ldots, 7\}$ and $t \in \{1, \ldots, 7\}$. For the position closed-loop control, let us define the switching function as

$$s_p = \frac{\ddot{e}_p}{\omega_p^2} + \frac{2\xi \dot{e}_p}{\omega_p} + e_p \tag{4.3}$$

in which $e_p = y_m - y_s$. It should be noted that the slave actuator controller uses this switching function (s_p) whereas the master actuator uses its negative ($-s_p$). To be able to analyze the closed-loop stability, consider the Lyapunov function candidate

$$V_{lya} = \frac{1}{2} s_p^2 \tag{4.4}$$

which is a positive-definite function. Therefore, if $\dot{V}_{lya} < 0$, then V_{lya} will be decreasing. If V_{lya} is decreasing, $|s_p|$ will also be decreasing. Assuming s_p is initially bounded and $|s_p|$ is always decreasing, then s_p will always be bounded. This means that s_p will approach zero if we control the system so that

$$\dot{V}_{lya} = \dot{s}_p \, s_p < -\eta_p |s_p| \tag{4.5}$$

for some positive constant $\eta_p > 0$ [32, 36, 37]. This condition can be rewritten as

$$\begin{cases} \dot{s}_p > \eta_p & \text{if } s_p < 0 \\ \dot{s}_p < -\eta_p & \text{if } s_p > 0 \end{cases} \tag{4.6}$$

In the above, $\dot{s}_p$ is found by taking the derivative of (4.3):

$$\dot{s}_p = \frac{\dddot{e}_p}{\omega_p^2} + \frac{2\xi \ddot{e}_p}{\omega_p} + \dot{e}_p \tag{4.7}$$

Let us consider two possible cases for the sign of $\dot{s}_p$ in the following.

- Assume that s_p is positive. Then, (4.6) reduces to

$$\dot{s}_p < -\eta_p \tag{4.8}$$

Based on the sliding-mode control outlined in Section 3.2, the master and slave dynamics become

$$\begin{aligned} \dddot{y}_m &= f_m - g_{v,m} + \dot{\tau}_h / M & v \in \{3, \ 5, \ 7\} \\ \dddot{y}_s &= f_s + g_{t,s} - \dot{\tau}_e / M & t \in \{2, \ 4, \ 6\} \end{aligned} \tag{4.9}$$

because, as noted earlier, the slave controller uses the switching function s_p while the master controller uses the switching function $-s_p$. Substituting (4.9) into (4.7), we find

$$\dot{s}_p = \lambda_p - (g_{v,m} + g_{t,s})/\omega_p^2 \tag{4.10}$$

where

$$\lambda_p = \frac{(f_m - f_s) + (\dot{\tau}_h + \dot{\tau}_e)/M}{\omega_p^2} + \frac{2\xi}{\omega_p} \ddot{e}_p + \dot{e}_p \tag{4.11}$$

Finally, by substituting (4.10) into (4.8) we find

$$(g_{v,m} + g_{t,s}) > (\lambda_p + \eta_p)\omega_p^2 \tag{4.12}$$

38

- Assume that s_p is negative. Then, (4.6) reduces to

$$\dot{s}_p > \eta_p \tag{4.13}$$

Based on the sliding-mode control outlined in Section 3.2, the master and slave dynamics become

$$\ddot{y}_m = f_m + g_{v,m} + \dot{\tau}_h/M \qquad v \in \{2,\ 4,\ 6\}$$
$$\ddot{y}_s = f_s - g_{t,s} - \dot{\tau}_e/M \qquad t \in \{3,\ 5,\ 7\} \tag{4.14}$$

Substituting (4.14) into (4.7), we find

$$\dot{s}_p = \lambda_p + (g_{v,m} + g_{t,s})/\omega_p^2 \tag{4.15}$$

where λ_p has been defined in (4.11). Also, substituting (4.15) into (4.13), we find

$$(g_{v,m} + g_{t,s}) > (\eta_p - \lambda_p)\omega_p^2 \tag{4.16}$$

Therefore, if the positive-valued functions $g_{i,m}$ and $g_{i,s}$ for $i \in \{2 - 7\}$ are sufficiently large, then the control strategy can satisfy condition (4.6) as long as λ_p is bounded. On the other hand, since all twelve functions $g_{i,m}$ and $g_{i,s}$ are proportional to C_{val}, the valve's mass flow rate constant in (2.12), then choosing a large enough valve will ensure that these scalar functions will be sufficiently large and thus the convergence to the sliding surface $s_p = 0$ over time is guaranteed (provided λ_p is bounded).

To show that λ_p is bounded, we consider the following dynamic models for the operator and the environment [20, 39]:

$$\tau_h = -M_h\ddot{y}_m - B_h\dot{y}_m - K_hy_m + \tau_h^*$$
$$\tau_e = M_e\ddot{y}_s + B_e\dot{y}_s + K_ey_s + \tau_e^* \tag{4.17}$$

where M_h, M_e, B_h, B_e, K_h, and K_e are positive values corresponding to the mass, damping and stiffness of the operator's hand and environment, respectively. The τ_h^* and τ_e^* are the continuous exogenous input forces from the operator and the environment, which have limited energy and as such are bounded. Substituting (4.17) into (4.1) yields

$$(M + M_h)\ddot{y}_m + (b_V + B_h)\dot{y}_m + K_hy_m$$
$$= A(P_{P,m} - P_{N,m}) + \tau_h^*$$
$$(M + M_e)\ddot{y}_s + (b_V + B_e)\dot{y}_s + K_ey_s$$
$$= A(P_{P,s} - P_{N,s}) - \tau_e^* \tag{4.18}$$

$P_{q,m}$ and $P_{q,s}$ are bounded between P_S and P_E, therefore the right hand sides (RHS) of the equations in (4.18) are bounded. Since the RHS of (4.18) is bounded, the left hand side

(LHS) becomes a second-order BIBO stable system (due to the positive coefficients) and, therefore, y_m and y_s are bounded. Rearranging (4.18), we get

$$(M + M_h)\ddot{y}_m + (b_V + B_h)\dot{y}_m$$
$$= A(P_{P,m} - P_{N,m}) + \tau_h^* - K_h y_m$$
$$(M + M_e)\ddot{y}_s + (b_V + B_e)\dot{y}_s$$
$$= A(P_{P,s} - P_{N,s}) - \tau_e^* - K_e y_s \tag{4.19}$$

We find that in (4.19), the RHS is bounded and the LHS is a first-order BIBO stable system in terms of piston velocity, therefore $\dot{y}_m$ and $\dot{y}_s$ are also bounded. Rearranging (4.18) again, we have

$$(M + M_h)\ddot{y}_m = A(P_{P,m} - P_{N,m}) + \tau_h^*$$
$$- K_h y_m - (b_V + B_h)\dot{y}_m$$
$$(M + M_e)\ddot{y}_s = A(P_{P,s} - P_{N,s}) - \tau_e^*$$
$$- K_e y_s - (b_V + B_e)\dot{y}_s \tag{4.20}$$

and, therefore, $\ddot{y}_m$ and $\ddot{y}_s$ are bounded as well. Since the positions (y_m, y_s), velocities $(\dot{y}_m, \dot{y}_s)$, accelerations $(\ddot{y}_m, \ddot{y}_s)$, and exogenous inputs (τ_h^*, τ_e^*) are all bounded, then by (4.17) τ_h and τ_e must also be bounded.

Since positions (y_m, y_s) are bounded, the chamber volumes $(V_{q,m}, V_{q,s})$ must also be bounded and non-zero. Thus, the derivatives of the pressures $(\dot{P}_{q,m}, \dot{P}_{q,s})$ which are functions of volume, pressure, velocity, and mass flow rate are bounded because all of the aforementioned functions are also bounded.

If we take the derivative of (4.20) we obtain

$$(M + M_h)\dddot{y}_m = A(\dot{P}_{P,m} - \dot{P}_{N,m}) + \dot{\tau}_h^*$$
$$- K_h \dot{y}_m - (b_V + B_h)\ddot{y}_m$$
$$(M + M_e)\dddot{y}_s = A(\dot{P}_{P,s} - \dot{P}_{N,s}) - \dot{\tau}_e^*$$
$$- K_e \dot{y}_s - (b_V + B_e)\ddot{y}_s \tag{4.21}$$

As noted earlier, the τ_h^* and τ_e^* are continuous and have limited energy, and as such their derivatives must be bounded. Therefore, the RHS of the above equations are bounded and, therefore, the third derivatives of the positions $(\dddot{y}_m, \dddot{y}_s)$ are also bounded. In addition, by taking the derivative of (4.17), we find that $\dot{\tau}_h$ and $\dot{\tau}_e$ are bounded.

In summary, $V_{q,m}$, $V_{q,s}$, y_m, y_s, $\dot{y}_m$, $\dot{y}_s$, $\ddot{y}_m$, $\ddot{y}_s$, $P_{q,m}$, $P_{q,s}$, $\dot{\tau}_h$, and $\dot{\tau}_e$ are all bounded, and so is λ_p. Since λ_p is bounded, condition (4.5) is met and thus s will converge to the sliding surface $s = 0$ in finite time. This leads to the closed-loop stable dynamics

$$\ddot{e}_p + 2\xi\omega_p\dot{e}_p + \omega_p^2 e_p = 0 \tag{4.22}$$

in which the position error, e_p, asymptotically tends towards zero.
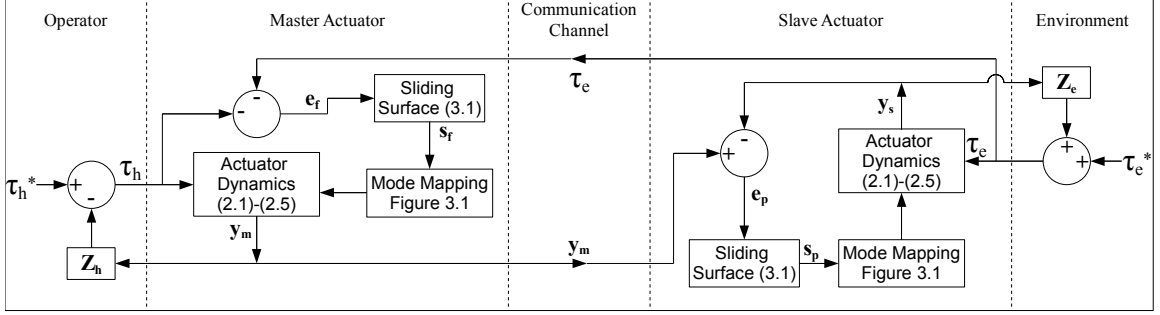
Figure 4.2: Force-position based teleoperation.

One of the distinct advantages of the position-position control architecture is that it does not require any force sensors for providing haptic feedback to the operator, but it comes at the cost of suffering from a distorted impedance perception in the free-motion condition and non-ideal force tracking [34].

4.2.2   Force-Position Control

The block diagram in Figure 4.2 shows the architecture for a force-position bilateral tele-operation system; the slave side of the system is identical to that in the position-position teleoperation case. As such, the slave actuator controller uses the same switching function (4.3) as in position-position architecture. It is still different because the sliding surface s_p is unrelated to the selected control action of the master. Therefore, the stability of the slave actuator will be the same as the single actuator stability analysis shown in Section 3.2.1.

Proving the stability for the closed-loop force-position control is very difficult; therefore in this section we will be providing a preliminary analysis of the system under force-position sliding-mode control. Force-position control is different from position-position control in that the control action for the master actuator comes from the readings of a sensor measuring slave/environment contact forces. Thus, the master's sliding-mode controller uses a new switching function s_f:

$$s_f = \frac{\ddot{e}_f}{\omega_f^2} + \frac{2\xi\dot{e}_f}{\omega_f} + e_f \tag{4.23}$$

where $e_f = -\tau_h - \tau_e$. To be able to analyze the closed-loop master system, consider the following Lyapunov function candidate

$$V_{lyb} = \frac{1}{2}s_f^2 \tag{4.24}$$

Evidently, V_{lyb} is a positive-definite function and, if $\dot{V}_{lyb} < 0$, V_{lyb} will be decreasing. If V_{lyb} is decreasing, $|s_f|$ will also be decreasing. Assuming s_f is initially bounded and $|s_f|$ is decreasing, s_f will approach zero. This requires that we control the master robot so that

$$\dot{V}_{lyb} = \dot{s}_f \, s_f < -\eta_f|s_f| \tag{4.25}$$

for some positive constant $\eta_f > 0$. This condition can be rewritten as

$$\begin{cases} \dot{s}_f > \eta_f & \text{if } s_f < 0 \\ \dot{s}_f < -\eta_f & \text{if } s_f > 0 \end{cases} \tag{4.26}$$

Take the derivative of (4.23) to obtain

$$\dot{s}_f = \frac{\dddot{e}_f}{\omega_f^2} + \frac{2\xi \ddot{e}_f}{\omega_f} + \dot{e}_f \tag{4.27}$$

- If we first consider that s_f is positive, according to (4.26) we have the following condition

$$\dot{s}_f < -\eta_f \tag{4.28}$$

Based on the sliding-mode control outlined in Section 3.2, the master and slave dynamics become

$$\dddot{y}_m = f_m - g_{t,m} + \dot{\tau}_h/M \qquad t \in \{3,\ 5,\ 7\}$$
$$\dddot{y}_s = f_s + (-1)^i g_{i,s} - \dot{\tau}_e/M \qquad i \in \{1 - 7\} \tag{4.29}$$

Substituting (4.29) into (4.27), we find

$$\dot{s}_f = \lambda_f - g_{t,m}M \tag{4.30}$$

where

$$\lambda_f = (-\dddot{y}_m + f_m - (-1)^i g_{i,s} + \dddot{y}_s - f_s)M + \frac{\dddot{e}_f}{\omega_f^2} + \frac{2\xi \ddot{e}_f}{\omega_f} \tag{4.31}$$

Also, substituting (4.30) into (4.28) we find

$$g_{t,m} > \frac{\lambda_f + \eta_f}{M} \tag{4.32}$$

- If we then consider that s_f is negative, according to (4.26) we have the following condition

$$\dot{s}_f > \eta_f \tag{4.33}$$

Based on the sliding-mode control outlined in Section 3.2, the master and slave dynamics become

$$\dddot{y}_m = f_m + g_{v,m} + \dot{\tau}_h/M \qquad v \in \{2,\ 4,\ 6\}$$
$$\dddot{y}_s = f_s + (-1)^i g_{i,s} - \dot{\tau}_e/M \qquad i \in \{1 - 7\} \tag{4.34}$$

Substituting (4.34) into (4.27) we find

$$\dot{s}_f = \lambda_f + g_{v,m}M \tag{4.35}$$

Finally, substituting (4.35) into (4.33) we find

$$g_{v,m} > \frac{\eta_f - \lambda_f}{M} \tag{4.36}$$

Therefore, if the positive-valued functions $g_{i,m}$ for $i \in \{2-7\}$ are large enough, the control strategy can satisfy condition (4.26). All six functions $b_{i,m}$ are proportional to C_{val}, the valve's mass flow rate constant in (2.12), thus choosing a large enough valve will ensure that these scalar functions will be sufficiently large, and thus, ensure the convergence to the sliding surface $s_f = 0$ within finite time.

4.3 Experimental Results

To test the teleoperation control schemes discussed previously, a quasi-periodic input motion pattern was applied by the operator's hand to the master. This input resembled three cycles of back-and-forth motion with an approximately 10 mm RMS amplitude when the slave was in free space, followed by approximately two seconds of motion causing contact between the slave and the environment, which was a soft material located 14.5 mm away from the slave's zero position. This entire motion pattern was repeated three times over a 20 second period by the human operator. The position and force profiles of the master and the slave robots were measured via position and force sensors (see Figure 4.3).

4.3.1 Experimental Setup

Experiments were performed with a pair of 1-DOF pneumatic actuators as the master and the slave – see Figure 4.3. Each pneumatic actuator has the same physical characteristics as described in Section 3.4. The low friction cylinders (Airpel model M16D100D) have a 16 mm diameter and a 100 mm stroke. The piston and shaft mass is approximately $M = 900$ g.

The controller is implemented using a dSPACE board (DS1104), running at a sampling rate of 500 Hz. This sampling rate has been chosen according to the open/close bandwidth of the valves and to enable an acceptable tracking response. The experimental setup has the model parameters listed in Table 3.4.

4.3.2 Position-Position Based Teleoperation Control

In this section, we review the experimental results for the position-position architecture using the sliding-mode control design in Section 4.2.1. For this experiment, the following controller parameters were selected: $\omega_p = 50$ rad/s, $\epsilon_p = 1$ mm, $\beta = 3.4$ mm, and $\tau = 40$ ms. The position-position scheme relied either on the 3-mode or the 7-mode based sliding control. The results are depicted in Figure 4.4. From these results, we can see that there is a 58% improvement in the RMS error of position tracking with the 7-mode based control compared to the 3-mode based control.

The force tracking performance is approximately the same for the 3-mode and the 7-mode control schemes as it is evident from Figure 4.4. When the slave is in contact with the environment ($\tau_e \neq 0$), there is good force tracking as $\tau_h \approx \tau_e$. However, under the free
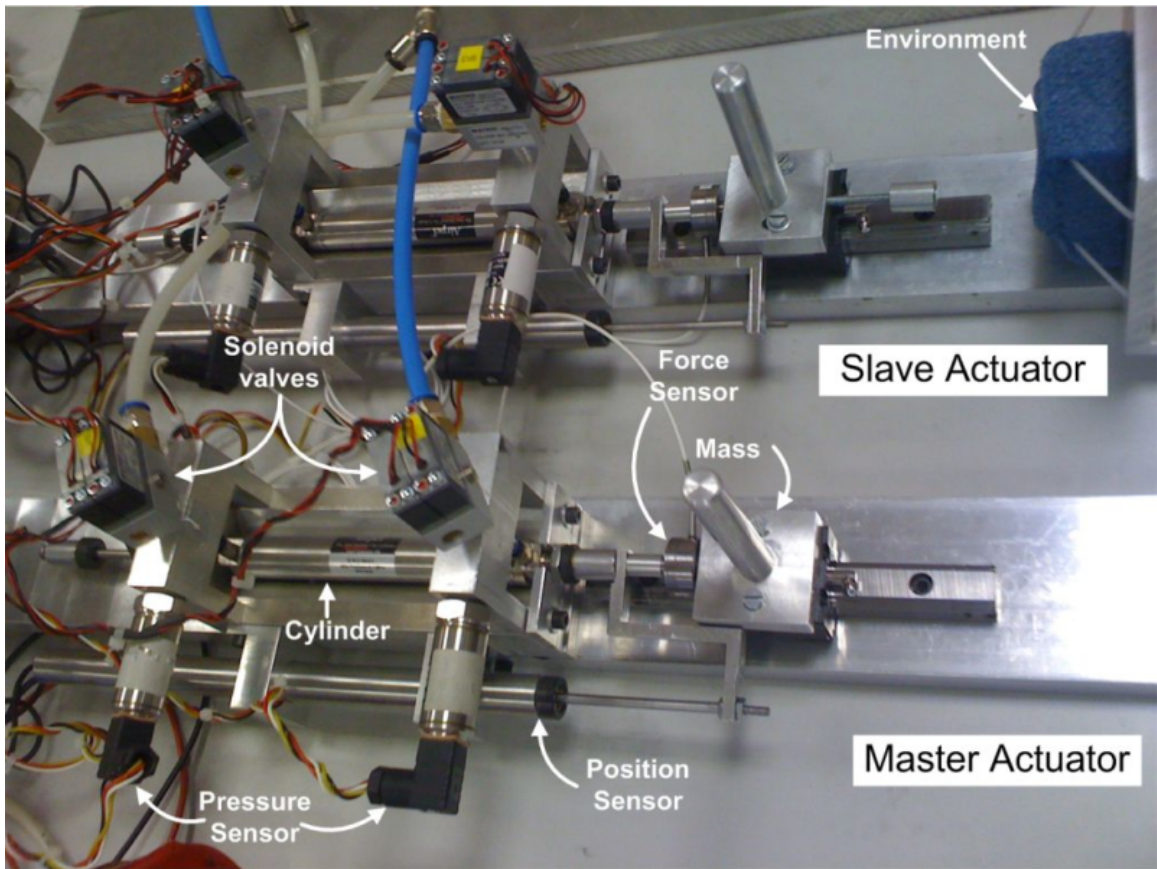
Figure 4.3: Experimental setup – pair of actuators.
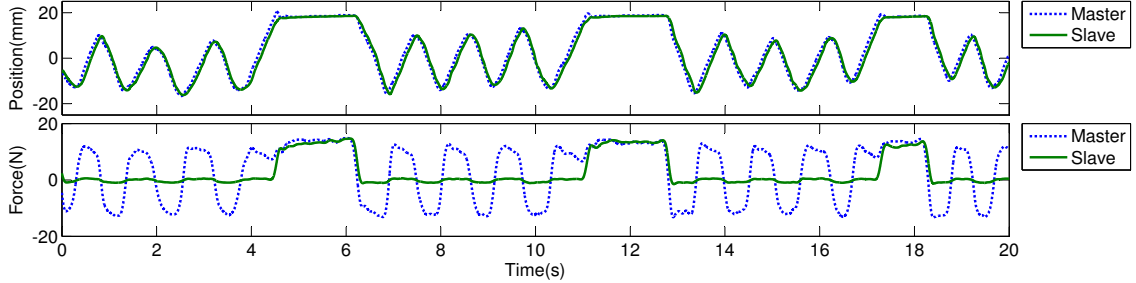
(a) with 3-Mode sliding control
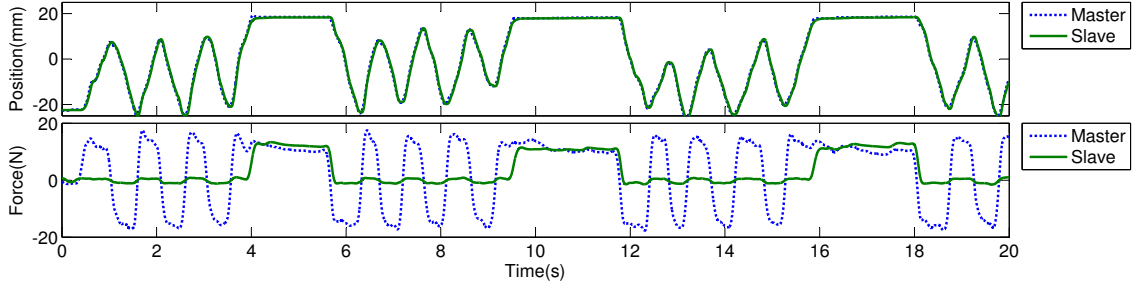
(b) with 7-Mode sliding control

Figure 4.4: Position and force tracking profiles for the master and the slave robots in position-position architecture.

motion case, (i.e., when $\tau_e \approx 0$, because the slave is not in contact with the environment), we see a sizable force feedback of about $+/-10$ N applied by the master to the operator.

4.3.3 Position-Force Based Teleoperation Control

In this section we review the experimental results for the force-position architecture defined in Section 4.2.2. For this experiment, the following force controller parameters were selected for the master controller: $\omega_f = 50$ rad/s, $\epsilon_f = 0.5$ N, $\beta = 1.7$ N, and $\tau = 40$ ms. The slave controller utilized the same control parameters described in Section 4.3.2. The force-position based control scheme was applied to both 3-mode and 7-mode based control. The results are charted in Figure 4.5. From these results we can see that there is a 44% improvement in position tracking error and a 20% improvement in force tracking error for the 7-mode based control when compared to the 3-mode based control under force-position based control.

4.4 Analysis and Discussion

4.4.1 Position-Position Based Teleoperation Control

In this section, we analyze the experimental results for the position-position architecture found in Section 4.3.2. The results are depicted in Figure 4.4. From these results we can observe reasonable position tracking. It also demonstrates good force tracking under the

(a) 3-Mode

(b) 7-Mode
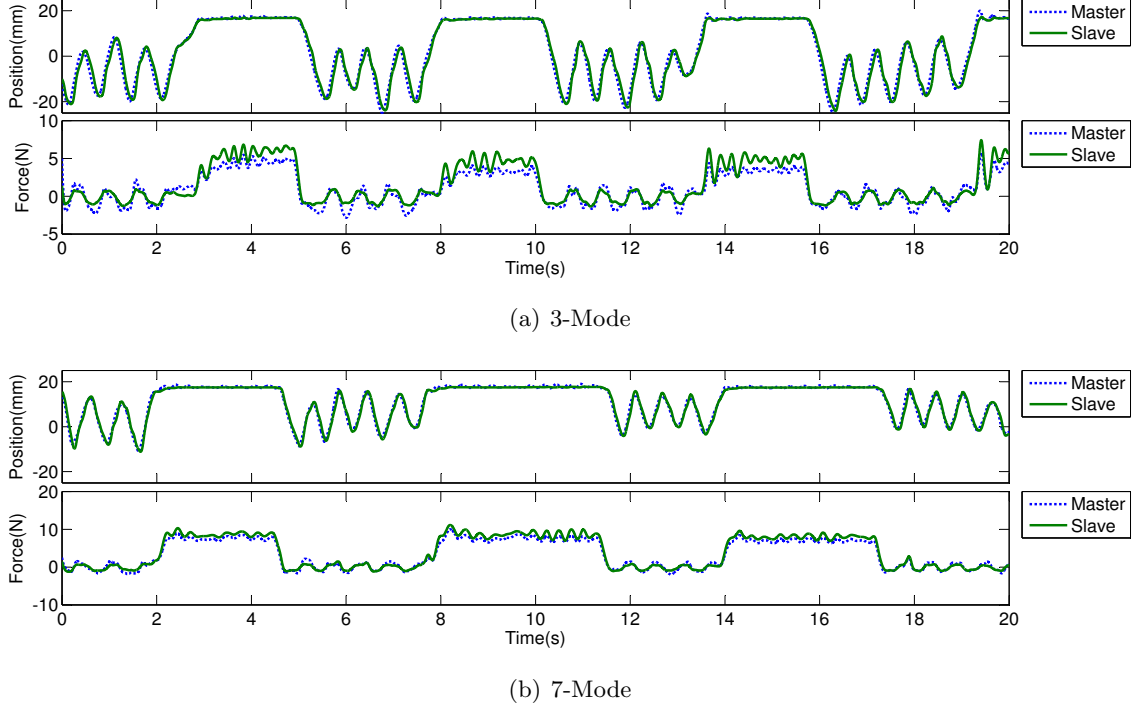
Figure 4.5: Sliding-mode control - force-position control.

case where it is in contact with the environment.

However, under the free motion case (i.e., while $\tau_e \approx 0$), because the slave is not in contact with the environment, we see a sizable force feedback of about ± 10 N applied by the master to the operator. This severely disrupts the perception of free motion for the operator and is undesirable. In the following, we try to understand the cause of this unwanted force feedback to the operator.

To illuminate the reason for the large force of ± 10 N experienced by the operator when the slave is in free space, let us examine the sum of forces acting on each actuator. The sum of forces according to (2.13) are

$$M\ddot{y}_s = -\tau_e + \tau_s - \tau_{F,s} \tag{4.37}$$

$$M\ddot{y}_m = \tau_h + \tau_m - \tau_{F,m} \tag{4.38}$$

where $\tau_s = (A_P P_{P,s} - A_N P_{N,s})$ is the slave actuator force, $\tau_m = (A_P P_{P,m} - A_N P_{N,m})$ is the master actuator force, $\tau_{F,s} = b_V \dot{y}_s$ is the slave damping force, and $\tau_{F,m} = b_V \dot{y}_m$ is the master damping force. First, consider the slave actuator in the free motion case where $\tau_e = 0$. We have

$$\tau_s = M\ddot{y} + \tau_{F,s} \tag{4.39}$$

In position-position control, the master's control action actuator is in the opposite direction to that of the slave:

$$\tau_m = -\tau_s \tag{4.40}$$

46
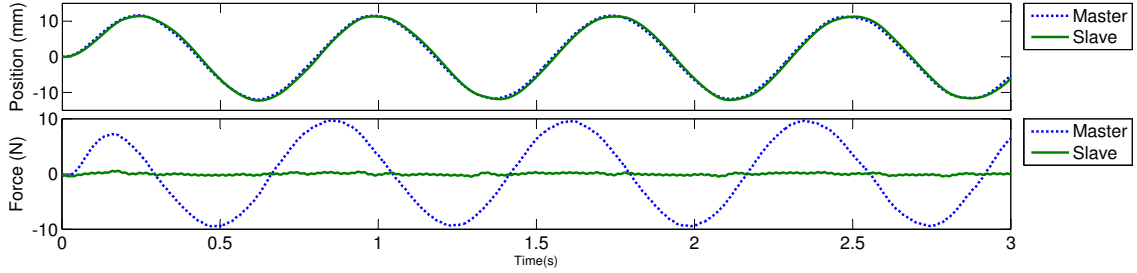
Figure 4.6: Position-position 7-mode simulated results

Substituting (4.39) into (4.40) gives us

$$\tau_m = -M\ddot{y} - \tau_{F,s} \tag{4.41}$$

Substituting (4.41) into (4.38) and solving for τ_h leads to

$$\tau_h = M(\ddot{y}_m + \ddot{y}_s) + \tau_{F,m} + \tau_{F,s} \tag{4.42}$$

In the experiments, the peak velocity is $\dot{y}_m \approx \dot{y}_s = 100$ mm/s and $b_V = 50$ N s/m. Therefore, the peak force of friction will be $\tau_{F,m} \approx \tau_{F,s} = 5$ N or a total unwanted force of $\tau_{F,m} + \tau_{F,s} = 10$ N. Therefore, it is the viscous friction that is causing a heavy loading in terms of the haptic feedback to the operator when the slave is in free space. This is a serious shortcoming of using the position-position control scheme for the pneumatic actuators.

To further evaluate this phenomenon we simulated in Simulink the free motion teleoperated case using Simulink. The results of this simulation are shown in Figure 4.6. These results also demonstrate a $\pm$ 10 N force, which corroborates with the analytical and experimental results.

For the case where the slave actuator is in contact with the environment ($\tau_e \neq 0$) the hand was stopped by the force feedback and, as a result the velocity decreased to near zero. Since the unwanted force is caused by the viscous friction, which is proportional to the actuators velocity, the unwanted force disappeared as their velocities went towards zero.

4.4.2 Force-Position Based Teleoperation Control

In this section, we analyze the experimental results for the force-position architecture found in Section 4.3.3. The results are depicted in Figure 4.5. From these results we can observe both in contact and under free motion that the haptic feedback to the master demonstrates good force tracking $\tau_h \approx \tau_e$ and position tracking. The force-position control scheme with pneumatic actuators does not have the sizable force feedback in free-motion that was observed in the position-position control scheme.

The force controller on the master side used the force sensor on the actuator in the control loop in such a way that the net force of the actuator ($\tau_m - \tau_{F,m}$) is equal to the force measured on the slave side.

47

As a result, the haptic feedback on the master side compensates for the force of friction on the master actuator. The force measured by the slave actuator does not include the force of friction on the slave side. Therefore, the only feedback felt by the hand through the haptic interface in the force-position free motion case is the inertia of the slave actuator.

This makes the force-position teleoperation architecture more advantageous then the position-position teleoperation architecture in terms of free motion force tracking. Although the force-position had better force tracking, it was observed that the position-position control architecture had a 16% improvement in position tracking when compared to the force-position control architecture.

4.5   Concluding Remarks

The seven-mode sliding-mode control law was originally designed in Chapter 3 for use on a single 2-chamber pneumatic actuator driven by on/off solenoid valves. In this chapter, the 7-mode control law was utilized in two teleoperation architectures: position-position and force-position. These closed-loop controls were experimentally verified on a setup consisting of a pair of symmetric pneumatic actuators. For comparison, the experiments were conducted for both the new 7-mode control and the traditional 3-mode control.

It was demonstrated that, for both teleoperation architectures, there was a 44%-58% improvement in position tracking error with the 7-mode controller when compared to the 3-mode controller. It was also demonstrated that there was a 20% improvement in force tracking error for the 7-mode controller in the force-position architecture when compared to the 3-mode controller in the same architecture.

In the position-position architecture, it was found that dynamic friction forces were causing large force applications (±10N) on the operator hand under the free motion case ($\tau_e = 0$). Thus, in terms of force tracking error, the force-position architecture is preferable for pneumatic actuators. The 7-mode based teleoperation control has performed well in the experiments. This controller would be a viable choice for use whenever a teleoperated robot uses on/off valves for actuation of the pneumatic chamber.

Chapter 5

Model-Based Pulse-Width-Modulated Sliding-Mode Control

5.1 Introduction

In Chapter 3, a sliding-mode control for a single pneumatic actuator was developed. In Chapter 4, the single pneumatic actuator control was extended to bilateral control of a pair of pneumatic actuators. Both of these control methods utilize a sliding-mode control derivation that involves mapping the various modes of pneumatic actuation to distances from the sliding surface. However, there are other methods for implementation of sliding-mode control.

In this chapter, we investigate utilizing model-based sliding-mode control on both a single actuator and a pair of bilaterally controlled actuators. Model-based sliding-mode control utilizes a controlled continuous input u in one of two ways: such that $\dot{s} = 0$, where s is an nth order integral switching function; or alternatively the continuous input u is chosen such that $\dot{s} \leq -\eta \, \text{sign}(s)$. To create a continuous-input model, a pulse-width-modulated (PWM) input signal is applied to the on/off solenoid valves. Under this control input, the discontinuous-input system is approximated via time-averaging as a continuous-input model.

This method has previously been applied to single actuator position control for three-mode control in [29]. In this thesis, we investigate expanding it from three-mode control to seven-mode control. To accomplish this, we had to create a new mode mapping for a time-averaged model, and recreate the controller accordingly. To expand the time-averaged model, we required additional regions in the levels of actuation, as well as the creation of different "profiles" of operation.

The organization of this chapter is as follows: The chapter introduction is in Section 5.1. An averaged continuous-input model of the open-loop actuator is described in Section 5.2. A sliding-mode control of a single pneumatic actuator is illustrated in Section 5.3. A sliding-

mode control of a teleoperated pair of solenoid-valve actuators is listed in Section 5.4. The experimental results are shown in Section 5.5. Finally, the concluding remarks are presented in Section 5.6.

5.2 Averaged Continuous-Input Model of the Open-Loop Actuator

Let us consider a general dynamic system that may operate in one of p distinct modes at any given time. Within a "period", (to be defined later), the system can switch between modes 1 through p. Perhaps this is due to the particular control input provided to the system according to the modal duty cycle d_i where

$$D = [d_1, d_2, ..., d_p]^T \tag{5.1}$$

We call D the PWM period. This indicates that the total duration of the modal duty cycles must equal the total PWM period, which is usually normalized to unity, i.e., $||D||_1 = 1$. If the system has dynamics $y^{(n)} = f_i$ in mode i, and we collect the system dynamics for the p modes in the vector

$$F = [f_1, f_2, ..., f_p]^T \tag{5.2}$$

then an average model $y_a^{(n)}$ of the system dynamics $y^{(n)}$ can be approximated by [6, 29]

$$y_a^{(n)} = F^T D \tag{5.3}$$

5.2.1 Duty Cycle Mapping for the 3-Mode System

Shen *et al.* have applied such a nonlinear model averaging to a 3-mode pneumatic actuator [29]. We will first derive that averaged model and then extend the method to the case of a 7-mode actuator. Using (2.15) for a single pneumatic actuator without external disturbances, we have

$$f_i = \begin{cases} f & , \ i = 1 \\ f + (-1)^i g_i & , \ \text{otherwise} \end{cases} \tag{5.4}$$

for $i \in \{1, 6, 7\}$ because, as discussed previously, these are the three modes corresponding to "Close and Close" (mode 1), "Push and Pull" (mode 6), and "Pull and Push" (mode 7). For creating a wide range of desired accelerations for the piston of the pneumatic actuator in the positive direction, we will want to appropriately mix modes 1 and 6. Similarly, for creating a wide range of desired piston accelerations in the negative direction, we will want to appropriately mix modes 1 and 7. To this end, within each of the positive and negative actuation regions, we can select a duty cycle based switching scheme that alternates between no actuation (mode 1) and full action (modes 6 and 7, respectively) [29]. Such a switching scheme is shown in Table 5.1 where
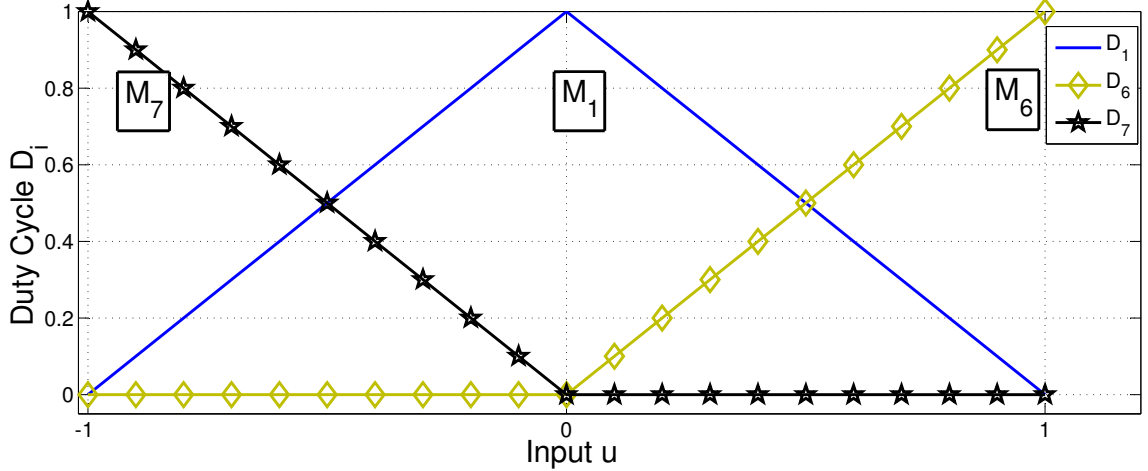
Figure 5.1: Duty cycle mapping for the 3-mode system.

$$d(u) = \frac{u_H - u}{u_H - u_L} \tag{5.5}$$

with $u_L \leq u \leq u_H$. Note that Table 5.1 leads to $u = 1$ and $u = -1$ corresponding to the maximum actuation in the positive and negative directions, respectively. Also, $u = 0$ will correspond to no actuation. Substituting (5.4) and Table 5.1 into (5.3), the average system model can be described by

$$\ddot{y}_a = \begin{cases} f + g_6 u & , \text{if } u \geq 0 \\ f + g_7 u & , \text{if } u < 0 \end{cases} \tag{5.6}$$

Table 5.1: The 3-mode mapping profile.

Region	u_L	u_H	Duty Cycles
-	-1	0	$d_7 = d(u)$, $d_1 = 1 - d(u)$
+	0	1	$d_1 = d(u)$, $d_6 = 1 - d(u)$

The switching between modes 1 and 6 or modes 1 and 7 according to Table 5.1 is illustrated in Figure 5.1 as a function of the input u. Figure 5.2 shows (5.6) in the plane containing $\ddot{y}_a - f$ versus u.

5.2.2 Duty Cycle Mapping for the 5-Mode System

If we extend the accepted values for the index i in (5.4) to be $i \in \{1, 2, 5, 6, 7\}$, the system will include two more control options: "Push and Close" (mode 2) and "Close and Push" (mode 5). This mapping will result in a 5-mode system.

For a 5-mode system, similar to the 3-mode system, we need to know the scheme for switching between modes. This new mode selection scheme involves a new mapping of the single input u to the duty cycle vector D. A desirable mapping would utilize at most two
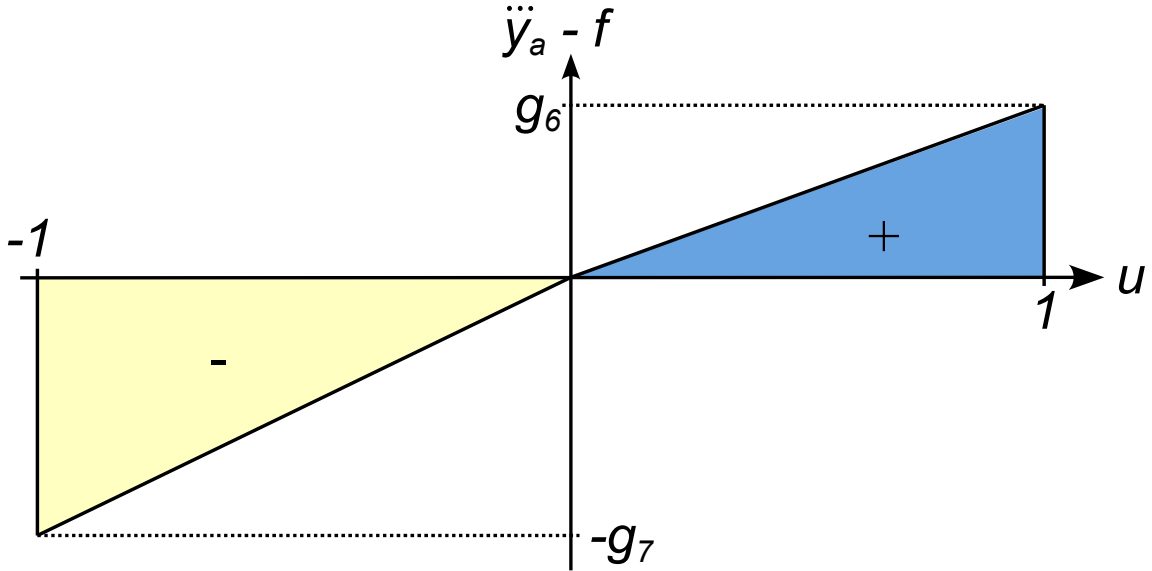
Figure 5.2: Theoretical time-averaged input-output relationship for the 3-mode system.

modes in any PWM period to simplify the mapping and also minimize the valves' switching for reduced noise and extended lifespan of the valves. Based on (5.4) and because g_i in (2.15) are all positive, we can see that the open-loop modes can be ordered in terms of the magnitude of the resulting $\dddot{y}$ for each mode:

$$f_7 \leq f_5 \leq f_1 \leq f_2 \leq f_6 \tag{5.7}$$

Given this order of actuation for each mode, it is beneficial to arrange the duty cycles as shown in Table 5.2. Utilizing these mappings, the output $\dddot{y}_a$ is increasing (decreasing) with increasing (decreasing) u, only two modes are used at a time, and $||D||_1 = 1$. The mapping from Table 5.2 is plotted in Figure 5.3.

To properly select the values of γ_2 and γ_5 in Table 5.2 we need to consider Figure 5.3. Figure 5.3 has four regions matching the same regions as in Table 5.2. At $u = 0$, mode 1 is utilized 100% of the time. As u decreases into the negative values (region 2), mode 5 is utilized increasingly until $u = -\gamma_5$, at which point mode 5 is utilized 100% of the time. As u further decreases (region 1), mode 5 is used increasingly less, and mode 7 is utilized increasingly until $u = -1$, at which point mode 7 is utilized 100%. The same holds for the positive range of u corresponding to regions 3 and 4 in Table 5.2. Additionally, if we select the following values for the transition points γ_2 and γ_5

$$\gamma_2 = \frac{g_2}{g_6} \qquad \gamma_5 = \frac{g_5}{g_7}$$

then we can see from Figure 5.4 that the resulting dynamics will have a continuous line across the transition points. It should be noted that any other selection of γ_2 and γ_5 will lead to a non-uniformity in terms of actuation, which will not be beneficial to the controller
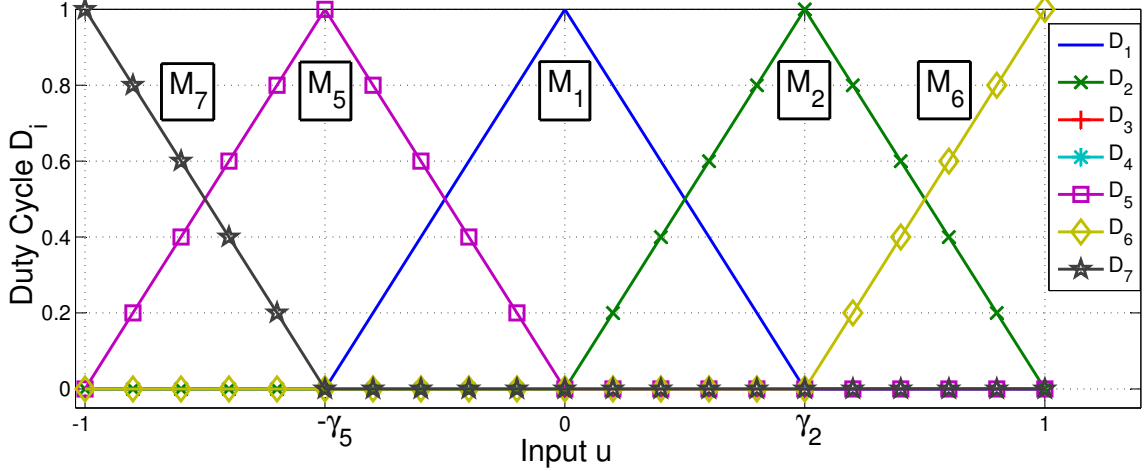
Figure 5.3: Duty cycle mapping for 5-mode.

design; refer to Figure 5.5. Note that since g_i in (2.15) are time-varying functions, γ_2 and γ_5 will also be functions of time.

Table 5.2: The 5-mode mapping profile.

Region	u_L	u_H	Duty Cycles
1	-1	$-\gamma_5$	$d_7 = d(u)$, $d_5 = 1 - d(u)$
2	$-\gamma_5$	0	$d_5 = d(u)$, $d_1 = 1 - d(u)$
3	0	γ_2	$d_1 = d(u)$, $d_2 = 1 - d(u)$
4	γ_2	1	$d_2 = d(u)$, $d_6 = 1 - d(u)$

The derivation of the time-averaged 5-mode model is shown in Appendix A.1. This derivation shows that, for the 5-mode system, the time-averaged model is the same as that for the 3-mode system. This is distinctly advantageous because we could use the same control input u for both 3-mode and 5-mode systems. The only difference between 3-mode and 5-mode operation is in the resulting valve open/close activity for a given u.

5.2.3 Duty Cycle Mapping for the 7-Mode System

If we extend the accepted values for the index i in (5.4) to be $i \in \{1, \ldots, 7\}$, the system will include two more control options: "Pull and Close" (mode 4) and "Close and Pull" (mode 3). This mapping will result in a 7-mode system.

For a 7-mode system, similar to the 5-mode system, a desirable mapping would utilize at most two modes in any PWM period. To properly evaluate the averaged model of the system, we will consider the 7-mode mapping through two separate mappings: The pressurizing profile (which utilizes modes M_7, M_5, M_1, M_2, and M_6) and the venting profile (which utilizes modes M_7, M_3, M_1, M_4, and M_6). Note that the mode selection scheme in the pressurizing profile in the 7-mode case is the same as that in the 5-mode case. Based on

Figure 5.4: Theoretical time-averaged input-output relationship for the 5-mode system.

Figure 5.5: Theoretical time-averaged input-output relationship for the 5-mode system with $\gamma_2 \neq g_2/g_6$ and $\gamma_5 \neq g_5/g_7$.
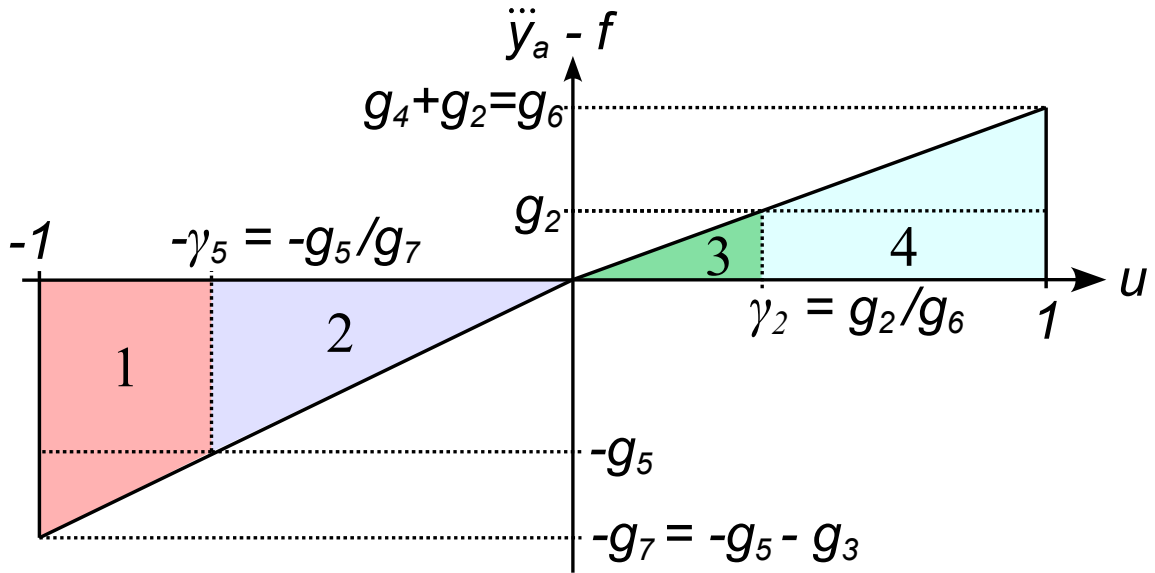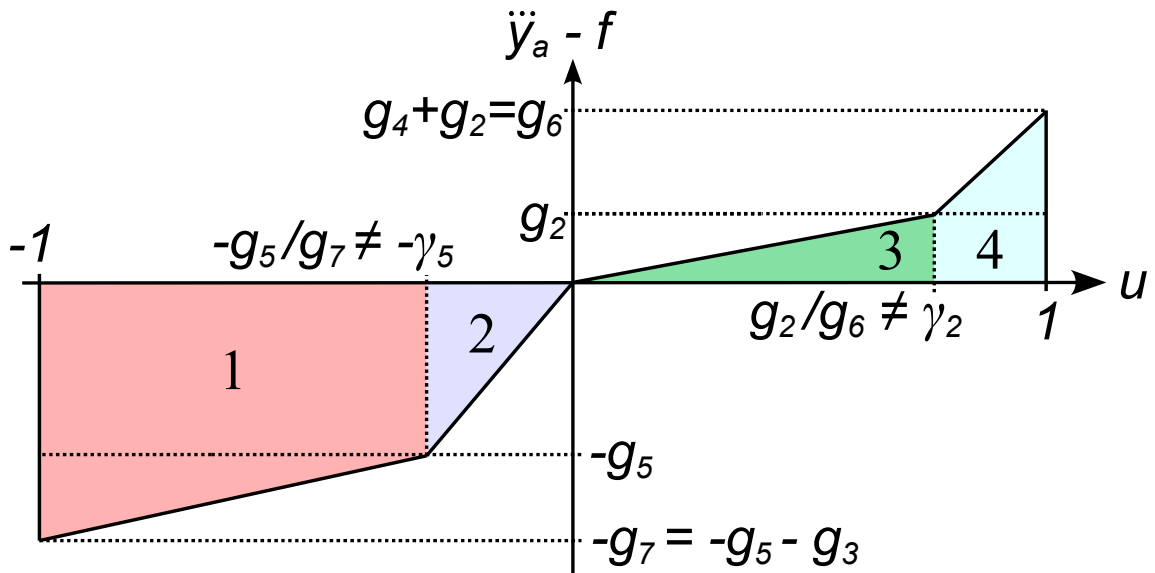
(5.4) and because g_i in (2.15) are all positive, we can see that these modes can be ordered in terms of the magnitude of the resulting $\dddot{y}$ for each mode:

$$\text{Pressurizing Profile:} \quad f_7 \le f_5 \le f_1 \le f_2 \le f_6$$
$$\text{Venting Profile:} \quad f_7 \le f_3 \le f_1 \le f_4 \le f_6$$

Given this order of actuation for each mode, it is beneficial to arrange the duty cycles as shown in Table 5.3. Observe that for the pressurizing profile we utilize both the same modes and the same mapping as the 5-mode mapping in the previous section.

Utilizing these mappings, the output $\dddot{y}_a$ is increasing (decreasing) with increasing (decreasing) u, only two modes are used at a time, and the $||D||_1 = 1$. The mapping in Table 5.3 is plotted in Figure 5.6(a) and 5.6(b).

We selected the same values for the transition points γ_2 and γ_5 as in 5-mode (see (5.8)). Applying the same methodology to the venting profile, we can select the following values for the transition points γ_4 and γ_3 in the venting profile:

$$\gamma_4 = \frac{g_4}{g_6} \qquad \gamma_3 = \frac{g_3}{g_7}$$

Using these values, we can see the resulting input-output relationship for the 7-mode system in the venting profile in Figure 5.7.

Table 5.3: The 7-mode profile mapping.

Pressurizing Profile			
Region	u_L	u_H	Duty Cycles
1	-1	$-\gamma_5$	$d_7 = d(u)$, $d_5 = 1 - d(u)$
2	$-\gamma_5$	0	$d_5 = d(u)$, $d_1 = 1 - d(u)$
3	0	γ_2	$d_1 = d(u)$, $d_2 = 1 - d(u)$
4	γ_2	1	$d_2 = d(u)$, $d_6 = 1 - d(u)$
Venting Profile			
Region	u_L	u_H	Duty Cycles
5	-1	$-\gamma_3$	$d_7 = d(u)$, $d_3 = 1 - d(u)$
6	$-\gamma_3$	0	$d_3 = d(u)$, $d_1 = 1 - d(u)$
7	0	γ_4	$d_1 = d(u)$, $d_4 = 1 - d(u)$
8	γ_4	1	$d_4 = d(u)$, $d_6 = 1 - d(u)$

The derivation of the time-averaged 7-mode model is shown in Appendix A. As it can be seen, the time-averaged model of the 7-mode system is the same as that for the 3-mode and 5-mode systems. So, we can use the same control input u for 3-mode, 5-mode and 7-mode systems.
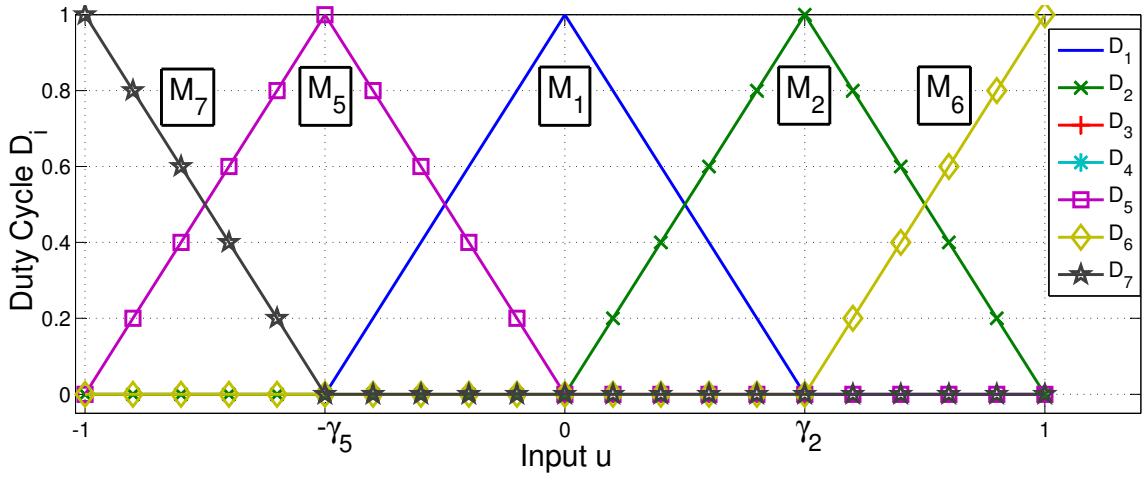
(a) 7-mode pressurizing.
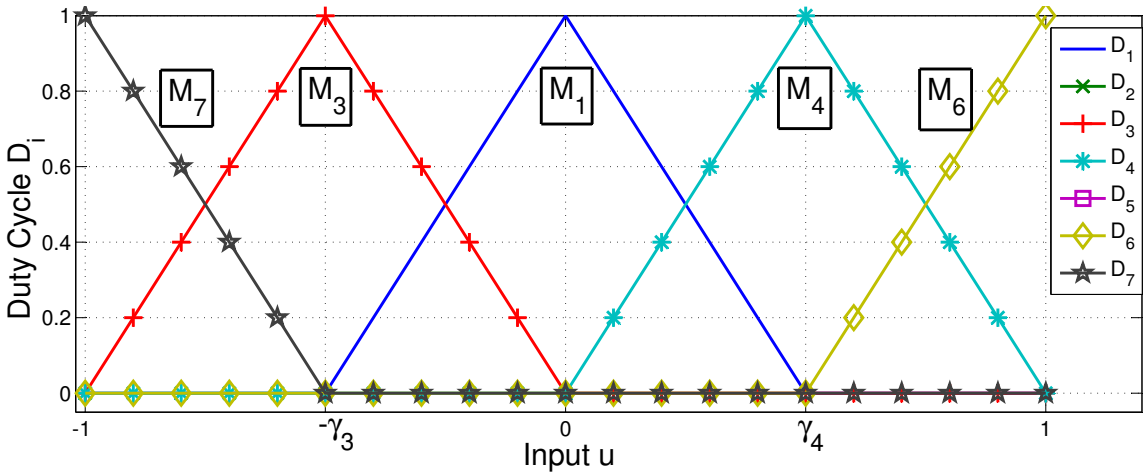
(b) 7-mode venting.

Figure 5.6: Duty cycle mapping.
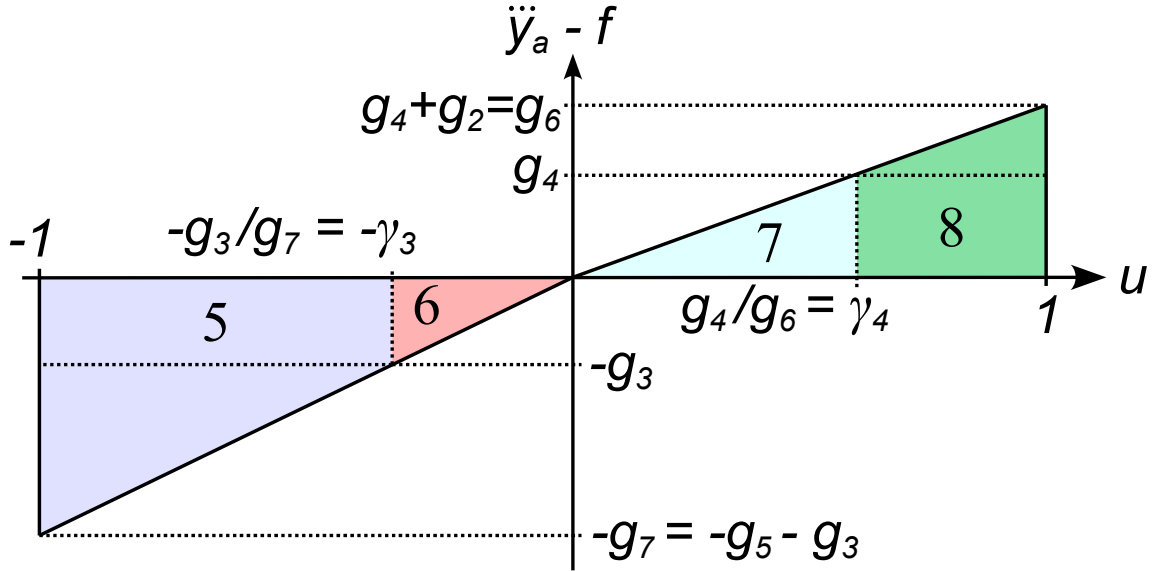
Figure 5.7: Theoretical time-averaged dynamics of the 7-mode venting.

5.3 Sliding-Mode Control of a Single Pneumatic Actuator

5.3.1 Position Control

Having expressed the multi-mode discrete-input system in a continuous input form (2.15), a sliding-mode approach can be applied for position control of the system. Selecting an integral sliding surface as

$$s_p = \left(\frac{d}{dt} + \omega_p\right)^3 \int_0^t e_p d\tau \tag{5.8}$$

where $e_p = y - y_d$ is the position error and ω_p is a positive gain, [29] develops a robust control law based on a sliding-mode approach, where the equivalent control action is derived by solving for the input when $\dot{s}_p = 0$. Taking the derivative of (5.8) we find

$$\dot{s}_p = \dddot{y} - \dddot{y}_d + 3\ddot{e}_p\omega_p + 3\dot{e}_p\omega_p^2 + e_p\omega_p^3 \tag{5.9}$$

if we substitute $\dddot{y}$ in (5.9) we obtain

$$\dot{s}_p = f + (g^{+/-})u - \dddot{y}_d + 3\ddot{e}_p\omega_p + 3\dot{e}_p\omega_p^2 + e_p\omega_p^3 \tag{5.10}$$

where

$$g^{+/-} = \begin{cases} g_6, \text{ if } u \geq 0 \\ g_7, \text{ if } u < 0 \end{cases}$$

Solving for u such that $\dot{s}_p = 0$ we find u_{eq} as

$$u_{eq} = \frac{\hat{u}}{g^{+/-}} \tag{5.11}$$

where

$$\hat{u} = \dddot{y}_d - f - 3\omega_p\ddot{e}_p - 3\omega_p^2\dot{e}_p - \omega_p^3 e_p \tag{5.12}$$

57

Utilizing the control (5.11) does not ensure convergence of the sliding surface in finite time, also the assumption $\ddot{y} = \ddot{y}_a$ is not correct. Thus to ensure robustness of the system we model the $\ddot{y}$ as a perturbed $\ddot{y}_a$ model.

Theorem 1 *Consider the perturbed system*

$$\ddot{y} = (1 + \Delta_f)f + (1 + \Delta_g)(g^{+/-})u \tag{5.13}$$

such that $|\Delta_f| \leq \alpha$ *and* $(\beta_{gm})^{-1} \leq (1 + \Delta_g) \leq \beta_{gm}$. *The control input*

$$u = \frac{\hat{u} - K\,sgn(s_p)}{g^{+/-}} \tag{5.14}$$

with the time-variant robustness gain K

$$K = \beta_{gm}(\alpha|f| + \eta_p) + (\beta_{gm} - 1)|\hat{u}| \tag{5.15}$$

will ensure convergence to the sliding surface $s_p = 0$ *in finite time (where* $\eta_p > 0$*).*

Proof.

To be able to analyze the closed-loop stability, consider the Lyapunov function candidate

$$V = \frac{1}{2}s_p^2 > 0 \tag{5.16}$$

If $\dot{V} < 0$, then V will be decreasing. If V is decreasing, $|s_p|$ will also be decreasing. Assuming s_p is initially bounded and $|s_p|$ is always decreasing, then s_p will be bounded and asymptotically approach zero. Thus, we intend to control the system so that

$$\dot{V} = \dot{s}_p s_p \leq -\eta_p|s_p| \tag{5.17}$$

If we analyze $\ddot{y}$ as a perturbed $\ddot{y}_a$, we can find $\ddot{y}$ as (5.13).

It should be noted that $\beta_{gm} \geq 1$. Substituting (5.13) and (5.12) into (5.9), we find

$$\dot{s}_p = (g^{+/-})u - \hat{u} + (\Delta_f)f + (\Delta_g)(g^{+/-})u \tag{5.18}$$

Using (5.14) and (5.18), we find

$$\dot{s}_p = -K\mathrm{sgn}(s_p) + (\Delta_f)f + (\Delta_g)(g^{+/-})u \tag{5.19}$$

Substituting (5.15) into (5.19), we find

$$\dot{s}_p = -\mathrm{sgn}(s_p)[\beta_{gm}(\alpha|f| + \eta_p) - \mathrm{sgn}(s_p)(\Delta_f)f + (\beta_{gm}-1)|\hat{u}| - \mathrm{sgn}(s_p)(\Delta_g)(g^{+/-})u] \tag{5.20}$$

Given that $(\beta_{gm}-1) \geq (\Delta_g)$, and $|\hat{u}| \geq \mathrm{sgn}(s_p)(g^{+/-})u$, we find that

$$(\beta_{gm}-1)|\hat{u}| - \mathrm{sgn}(s_p)(\Delta_g)(g^{+/-})u \geq 0 \tag{5.21}$$

and thus (5.20) can be simplified to

$$\dot{s}_p \leq -\text{sgn}(s_p)[\beta_{gm}(\alpha|f| + \eta_p) - \text{sgn}(s_p)(\Delta_f)f] \tag{5.22}$$

Given that $\beta_{gm} \geq 1$, and $\alpha \geq \Delta_f$, we find

$$\beta_{gm}\alpha|f| - \text{sgn}(s_p)(\Delta_f)f \geq 0 \tag{5.23}$$

And thus (5.22) can be simplified to

$$\dot{s}_p \leq -\beta_{gm}\eta_p\text{sgn}(s_p) \tag{5.24}$$

given that $\beta_{gm} \geq 1$

$$\dot{s}_p \leq -\eta_p\text{sgn}(s_p) \tag{5.25}$$

Multiply both sides of (5.25) by s_p and we obtain

$$\dot{s}_p s_p \leq -\eta_p|s_p| \tag{5.26}$$

The system will converge to the sliding surface $s_p = 0$ in finite time because the condition (5.26) satisfies (5.17). ∎

This leads to the closed-loop stable dynamics

$$\left(\frac{d}{dt} + \omega_p\right)^3 \int_0^t e_p d\tau = 0 \tag{5.27}$$

in which the position error e_p asymptotically tends towards zero.

Utilizing the control action u obtained from (2.16), (5.12), (5.14), and (5.15) we can apply the closed-loop control to a 3-mode system using the mapping from Table 5.1 or to a 7-mode system using the mapping from Table 5.3.

For the 7-mode mapping there are two separate profiles: the venting and pressurizing profiles. The selection between the pressurizing and venting profiles is updated periodically based on the larger output actuation g_i.

It should also be noted that the order of the two modes in any given PWM window was arranged to minimize overall switching activity. For example if a PWM window ended with mode M_1 and the next window contained the M_1 mode that mode was used at the start of the next window.

5.4 Sliding-Mode Control of a Teleoperated Pair of Solenoid-Valve Actuators

This section of the paper focuses on force-position architecture for closed-loop control. For the teleoperation system, we assume that master and slave dynamics will be the same as those described in Section 2.3. For different actuators, the common variables will be re-labeled as shown in Table 4.1.
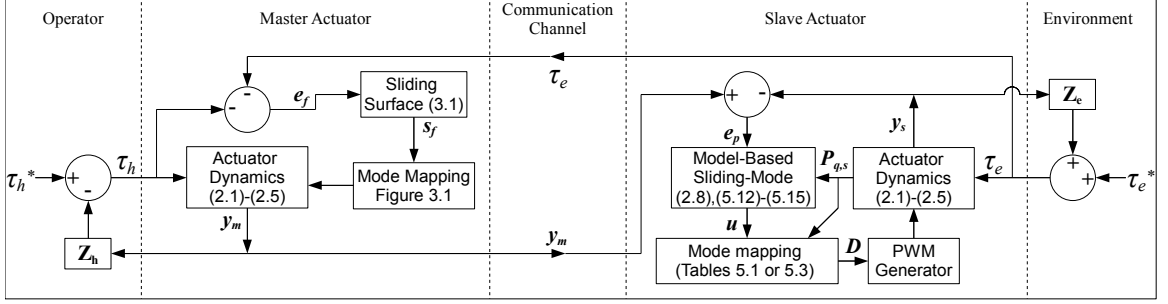
Figure 5.8: Force-position teleoperation control.

The block diagram in Figure 5.8 shows the architecture of a force-position bilateral teleoperation system. The slave side of the setup utilizes the model-based PWM sliding-mode control described in Section 5.3.1 where e_p is defined as $y_m - y_s$. The master side of the setup utilizes the switching function based control of position described in Section 4.2.2, where e_f is defined as $-\tau_h - \tau_e$.

5.5 Experimental Results

5.5.1 Experimental Setup

In this paper, experiments were performed with a pair of 1-DOF pneumatic actuators as the master and the slave (see Figure 4.3). Each pneumatic actuator has the same physical characteristics as described in Section 3.4. The low friction cylinders (Airpel model M16D100D) have a 16 mm diameter and a 100 mm stroke. The piston and shaft mass is approximately M = 900 g. The controller is implemented using a dSPACE board (DS1104), running at a sampling rate of 500 Hz. This sampling rate has been chosen according to the open/close bandwidth of the valves and to enable an acceptable tracking response. The experimental setup has the model parameters listed in Table 3.4.

5.5.2 PWM 7-Mode Single Actuator Position Control Results

This section outlines the experimental testing conducted using the 7-mode PWM single actuator controller. The following controller parameters were utilized: $\omega_p = 60$ rad/s, $\alpha = 0.1$, $\beta_{gm} = 1.1$, and $\eta_p = 100$ m/s^3 on (5.12), (5.14), and (5.15). The following sinewave test pattern was used to test the position tracking performance of the proposed algorithm:

$$y_d = 20\text{mm }\sin(2\pi f t) \tag{5.28}$$

The frequency was varied from 0.1 Hz to 3.0 Hz. The tracking performance and switching activity was evaluated for this test pattern over a 10 second period.

The results are plotted in Figure 5.9. From these results, we find that for both the 3-mode and the 7-mode systems, increasing the input frequency increases the RMS tracking

60
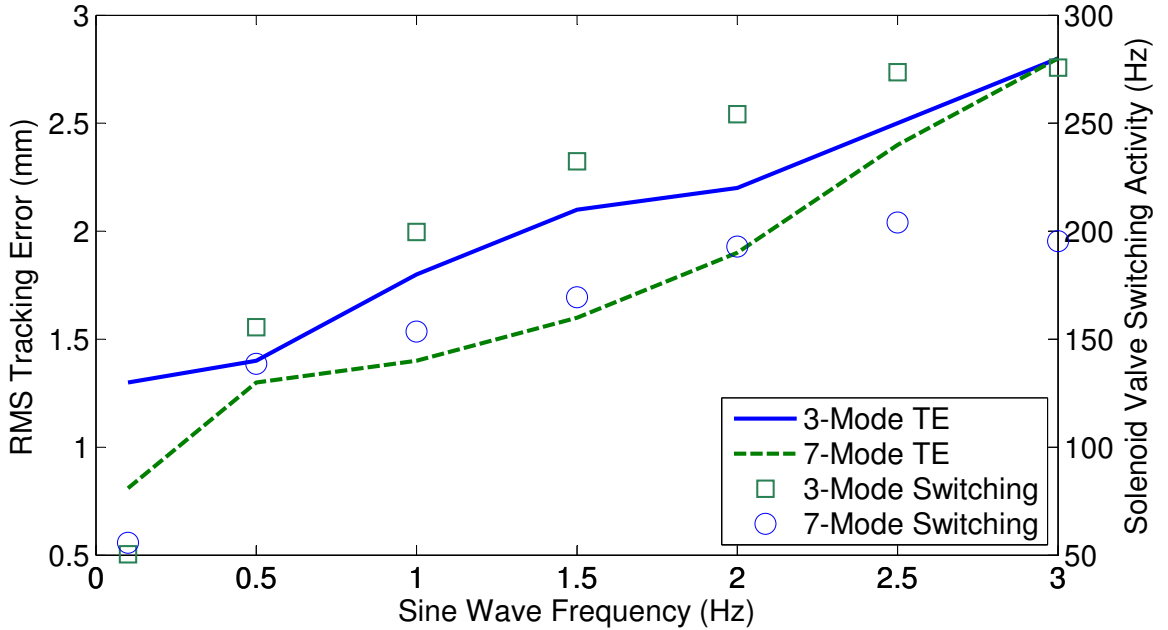
Figure 5.9: PWM tracking and switching performance of a single actuator with a sine wave input.

error. When we compare the results for the 3-mode controller and the 7-mode controller, we can see that there is a notable improvement in tracking performance for the 7-mode controller, as well as a notable decrease in switching activity in the 7-mode case.

5.5.3 Force-Position Teleoperation Control Utilizing PWM Position Control

In this section, we discuss the experimental results for the force-position architecture using the sliding-mode control design in Section 5.4. To test the teleoperation control scheme developed above, a quasi-periodic input motion pattern was applied by the operator's hand to the master. This input resembled three cycles of back-and-forth motion with an approximate 10 mm RMS amplitude when the slave was in free space, followed by approximately two seconds of motion causing contact between the slave and its environment. The slave's environment was a soft material located 14.5 mm away from the slave's zero position. This entire motion pattern was repeated three times over a 20 second period by the human operator. The position and force profiles of the master and the slave robots were measured via position and force sensors (see Figure 4.3).

For this experiment, the following parameters were selected for the master controller: $\omega_f = 50$ rad/s, $\tau = 40$ ms, $\epsilon = 0.5$N, $\beta = 1.7$N, and $\xi = 1$ on (4.23). The slave controller utilized the same control parameters described in Section 5.5.2.
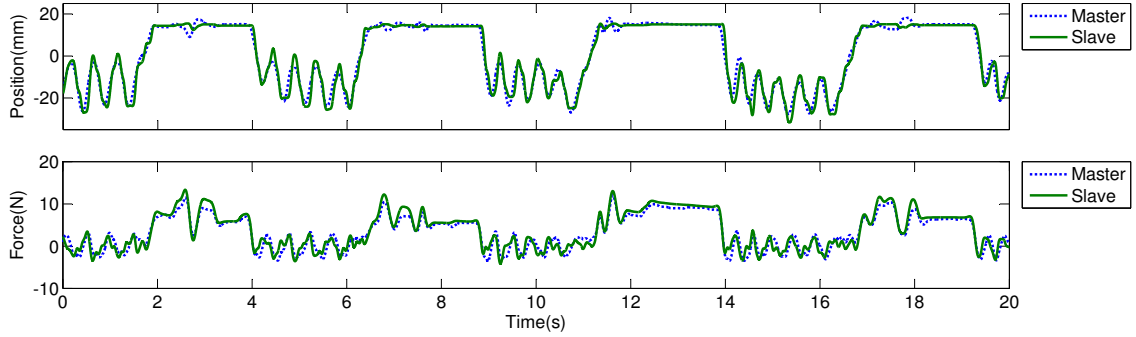
(a) 3-mode
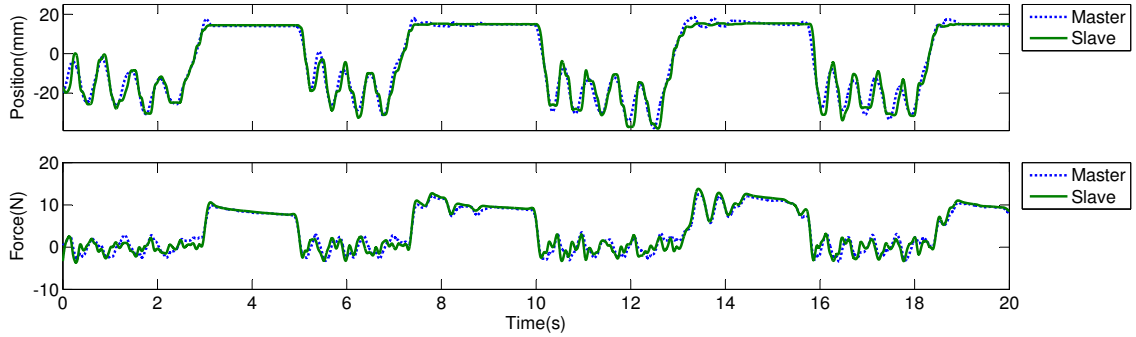
(b) 7-mode

Figure 5.10: Force-position control with PWM position control on the slave.

The force-position scheme relied either on the 3-mode or the 7-mode based sliding control of the slave actuator's position. The results are depicted in Figure 5.10. The slave actuator has a soft material located at 14.5 mm from it. When the operator tries to move the slave beyond the 14.5 mm position, the master reflects a force to the operator that is proportional to the measured contact force between the slave and the environment. Comparing the results between the 3-mode and the 7-mode cases in Figure 5.10, we can see that there is an 11% improvement in the RMS error of position tracking error and a 38% improvement in the RMS error of force tracking with the 7-mode based control compared to the 3-mode based control under force-position control.

When the slave actuator position's is less then 14.5 mm, the slave is in free motion. Under the free motion condition, (i.e., $\tau_e \approx 0$), the position tracking and force tracking were not found to significantly improve under the 7-mode based control when compared to the 3-mode based control under force-position control. Nonetheless, from the 3-mode to the 7-mode controller, there was a consistent 20% reduction in switching activity of the on/off solenoid valves, which increases their operating lifespan.

5.6   Concluding Remarks

A nonlinear model averaging approach was utilized that enabled the use of a full nonlinear model based control. This averaging method was applied to a PWM controlled pneumatic actuator with on/off solenoid valves. In this chapter, the 3-mode control law for a single pneumatic actuator was expanded for use in a 7-mode system. The 7-mode control results were compared experimentally against the 3-mode control results in terms of position tracking performance and switching activity. The results showed improved position tracking and reduced switching activity of the on/off solenoid-valves thus extending their lifespan for the 7-mode controller.

This 7-mode architecture was then expanded to a paired actuator setup utilizing a force-position teleoperation scheme. The teleoperation system performance was experimentally compared between the 7-mode and the 3-mode architectures. The transparency was evaluated based on the position tracking performance and the force tracking performance between the master and the slave robots. On contact, the 7-mode system was found to show an improvement in terms of position tracking, force tracking, and switching activity over the 3-mode system.

Thus, for both the single actuator and the paired actuator system, the performance was found to improve with the additional modes of actuation. These additional modes of operation provided by the 7-mode controller allowed for reduced, yet appropriate amounts of drive actuation. The outcome was more efficient actuator control, which provided the improved performance.

Chapter 6

Conclusions and Future Research

6.1 Conclusions

For the symmetric two chamber pneumatic actuator with four on/off solenoid valves, there are a total of sixteen operating modes. However, since we do not want to have a single chamber connected to both pressure and exhaust at the same time, seven of these modes are invalid. Therefore, there are a total of nine unique control possibilities. Past work has focused on 3-mode position control. In this thesis, we have investigated utilizing a 7-mode sliding-mode control law for precise position control and minimal switching activity in a pneumatic-actuated robot and telerobot. In order to develop a 7-mode sliding-mode control law, we developed new operating regions based on the distance from the sliding surface $s = 0$ to utilize the four new modes of operation. Implementing these new regions required new control parameters (β, τ) and tuning methods to obtain these parameters. In this thesis, these control methods were developed methodically.

A control algorithm for a seven-mode system was developed in Chapter 3. In order to evaluate the success of the proposed control strategy, a comparison has been performed relative to the three-mode controller in [18] for a position tracking problem. The results show that the tracking accuracy is better in the case of seven-mode control compared to the three mode control. The seven-mode controller also demonstrated a significant reduction in the switching of the solenoid valves compared to the three-mode.

For the single actuator case, an investigation into a time-varying threshold ϵ that is used to decide the transition between two modes was conducted theoretically and experimentally in Section 3.2.3 of Chapter 3. To evaluate the effect of the proposed time-varying threshold, a comparison study has been performed between a 'fixed ϵ' and a 'time-varying ϵ' on a step function position tracking problem. Using the time-varying ϵ successfully resulted in less settling time for the position response, leading to a notable improvement to tracking performance. It also caused a decrease in switching activity.

The seven-mode control was extended from the position control of a single robot to the bilateral control of a telerobot in Chapter 4. The seven-mode control law was utilized in two teleoperation architectures: position-position and force-position. These sliding-mode con-

trol architectures were verified using an experimental setup consisting of a pair of symmetric pneumatic actuators.

A comparison study has been performed relative to the traditional three-mode controller for the teleoperation case. For both teleoperation architectures, there was a 44%-58% improvement in the RMS position tracking error with the seven-mode controller. There was also a 20% improvement in the force RMS tracking error for the seven-mode controller.

Under the free motion case in the position-position teleoperation, there was a large unwanted force feedback (about ± 10 N) on the operator's hand. This was caused by the dynamic friction forces in the pneumatic actuators. On the other hand, the force-position architecture used slave-side force sensor measurements and, as a result, did not involve the large force feedback when the slave was in free motion. Thus, in terms of force tracking error, the force-position architecture is preferable compared to the position-position architecture.

Finally, in Chapter 5, nonlinear model-based sliding-mode control was investigated as an alternative method. The control methods developed in [29] were extended from the 3-mode system to the 7-mode system. Both the 3-mode and the 7-mode controllers were experimentally validated for both the single actuator and the pair of teleoperated actuators. The experimental results showed improved position tracking performance and reduced switching activity of the on/off solenoid valves, thus extending the valves' lifespan, for the 7-mode controller.

The 7-mode solenoid-valve pneumatic actuator has been successfully implemented first in simulations, and then in experiments; good control results have been achieved. Such a system would be an excellent choice for use as an actuator of an MRI-compatible robotic system because it does not have any metallic components and does not generate a magnetic field.

6.2 Suggestions For Future Research

The air hoses in a pneumatic system introduce time delay. In this thesis, we had neglected the time delays. In general, time delay may destabilize an otherwise stable system. As has been demonstrated in [22], a regular sliding-mode controller with some modification can control a slave system to perform a task well independently of time delay. Therefore, future research can explore using sliding-mode control to handle time delays in a pneumatic system.

Having studied the positive effects of 7-mode control (compared to 3-mode control) on positioning accuracy and switching activity in a teleoperation system, the next step could be investigating the effectiveness of 7-mode control in terms of high-fidelity transmission of critical haptic cues to the human operator. This can be done in the context of a delicate task such as needle insertion that is performed via a teleoperation system. In this task, the needle is to be inserted into a multi-layer tissue model (comprising of skin, fat, muscle, etc.) and the human operators need to detect the puncture of each tissue layer using haptic

feedback. In this task, low positioning accuracy or high switching activity can disrupt the perception of soft tissue for the operator. In this way, we can conduct experiments by which the performance of human operators in terms of task success rate and task completion times is compared for 7-mode versus 3-mode control. The ultimate test of transparency is the above-described subjective experiments.

In position-position teleoperation control, we found that viscous friction was being felt very heavily by the operator and this reduced the transparency of the teleoperation system. Future research can investigate the effect of feed-forward compensation of friction added to the sliding-mode pneumatic position-position teleoperation controller.

Appendix A

Time-Averaged Model for the 7-Mode System

The time-averaged model for the 7-mode PWM controller is derived by evaluating the combination of system dynamics. As noted, modes M_8 and M_9 are not utilized. Denoting the duty cycle vector as

$$D = [d_1 \ d_2 \ d_3 \ d_4 \ d_5 \ d_6 \ d_7]^T \tag{A.1}$$

and the modal system dynamics vector as

$$F = [f_1 \ f_2 \ f_3 \ f_4 \ f_5 \ f_6 \ f_7]^T \tag{A.2}$$

where

$$f_i = \begin{cases} f & , \ i = 1 \\ f + (-1)^i g_i & , \ \text{otherwise} \end{cases} \tag{A.3}$$

for $1 \geq i \geq 7$, the average system dynamics are given by (5.3) as

$$\ddot{y}_a = F^T D = \sum_{i=1}^{7} f_i d_i \tag{A.4}$$

Substituting (A.3) into (A.4) we find

$$\ddot{y}_a = f + \sum_{i=2}^{7} (-1)^i g_i d_i \tag{A.5}$$

Please note this model does not consider external disturbances for model based control because these are assumed to be unknown.

A.1   Pressurizing Profile

Defining the duty cycle vector as given by Table 5.3 we can evaluate the time-averaged model for the four regions for the pressurizing profile. To do this we evaluate the time-averaged

model's partial derivative with respect to the continuous input u

$$\frac{\partial(\dddot{y}_a)}{\partial u} = \sum_{i=2}^{7}(-1)^i g_i \frac{\partial d_i}{\partial u} \tag{A.6}$$

The d_i are defined by (5.5). Taking the derivative of (5.5) we find the slope to be

$$\frac{\partial d_{U1}(u)}{\partial u} = \frac{-1}{U_2 - U_1} = -m_d$$
$$\frac{\partial d_{U2}(u)}{\partial u} = \frac{1}{U_2 - U_1} = m_d \tag{A.7}$$

Using these equations, the derivatives for $\partial d_i/\partial u$ can be found for the four regions in the pressurizing profile (see Table A.1).

For region 1 $d_i = 0$ for $i \neq \{5,7\}$. Therefore, for this region the system dynamics are given by

$$\begin{aligned}
\frac{\partial(\dddot{y}_a)}{\partial u} &= -g_7\frac{\partial d_7}{\partial u} + -g_5\frac{\partial d_5}{\partial u} \\
&= -g_7(-\frac{g_7}{g_3}) + -g_5(\frac{g_7}{g_3}) \\
&= (g_7 - g_5)\frac{g_7}{g_3} = \cancel{g_5}\frac{g_7}{\cancel{g_5}} \\
&= g_7
\end{aligned} \tag{A.8}$$

Repeating this process for the other 3 regions we can find the time-averaged model's partial derivative with respect to the continuous input u as shown in Table A.1.

Table A.1: Pressurizing profile mapping (derivative).

Region	m_d	Modes	$\partial(\dddot{y}_a)/\partial u$
1	g_7/g_3	M_7, M_5	g_7
2	g_7/g_5	M_5, M_1	g_7
3	g_6/g_2	M_1, M_2	g_6
4	g_6/g_4	M_2, M_6	g_6

Thus, if we combine the results from Table A.1 and integrate then, we find the following time-averaged model:

$$\int_0^u \frac{\partial(\dddot{y}_a)}{\partial u} du = \begin{cases} g_6 u + C & \text{, if } u \geq 0 \\ g_7 u + C & \text{, if } u < 0 \end{cases} \tag{A.9}$$

Evaluating $C = \dddot{y}_a|_{u=0}$ we find that $C = f$. Substituting, we find the pressurizing time-averaged model to be:

$$\dddot{y}_a = \begin{cases} f + g_6 u & \text{, if } u \geq 0 \\ f + g_7 u & \text{, if } u < 0 \end{cases} \tag{A.10}$$

A.2   Venting Profile

Repeating the process from appendix A.1 using the duty cycle vector as given by Table 5.3, we can evaluate the time-averaged model for the four regions for the venting profile. Using these equations the derivatives in (A.7) for $\partial d_i / \partial u$ can be found for the four regions in the venting profile (see Table A.2). For region 5 $d_i = 0$ for $i \neq \{3, 7\}$. Therefore for this region, the system dynamics are given by

$$
\begin{aligned}
\frac{\partial(\dddot{y}_a)}{\partial u} &= -g_7 \frac{\partial d_7}{\partial u} + -g_3 \frac{\partial d_3}{\partial u} \\
&= -g_7(-\frac{g_7}{g_5}) + -g_3(\frac{g_7}{g_5}) \\
&= (g_7 - g_3)\frac{g_7}{g_5} = \cancel{g_5}\frac{g_7}{\cancel{g_5}} \\
&= g_7
\end{aligned}
\tag{A.11}
$$

Repeating this process for the other 3 regions we can find the time-averaged model's partial derivative with respect to the continuous input u as shown in Table A.2.

Table A.2: Venting profile mapping (derivative).

Region	m_d	Modes	$\partial(\dddot{y}_a)/\partial u$
5	g_7/g_5	M_7, M_3	g_7
6	g_7/g_3	M_3, M_1	g_7
7	g_6/g_4	M_1, M_4	g_6
8	g_6/g_2	M_4, M_6	g_6

Thus, if we combine the results from Table A.2 and integrate, we find the following time-averaged model:

$$
\int_0^u \frac{\partial(\dddot{y}_a)}{\partial u} du = \begin{cases} g_6 u + C & \text{, if } u \geq 0 \\ g_7 u + C & \text{, if } u < 0 \end{cases}
\tag{A.12}
$$

Evaluating $C = \dddot{y}_a\big|_{u=0}$ we find that $C = f$. Substituting we find the venting time-averaged model to be:

$$
\dddot{y}_a = \begin{cases} f + g_6 u & \text{, if } u \geq 0 \\ f + g_7 u & \text{, if } u < 0 \end{cases}
\tag{A.13}
$$

Comparing (5.6), (A.10), and (A.13) we find they are all the same. Since they have the same time-averaged model they can use the same sliding surface switching function, s_p, see (5.8), the same robustness gain, K, see (5.15), and thus the same continuous closed-loop control, u, see (5.14).

Bibliography

[1] K. Ahn and S. Yokota, "Intelligent switching control of pneumatic actuator using on/off solenoid valves," *Mechatronics*, vol. 15, no. 6, pp. 683–702, 2005.

[2] R. O. Ambrose, H. Aldridge, R. S. Askew, R. R. Burridge, W. Bluethmann, M. Diftler, C. Lovchik, D. Magruder, and F. Rehnmark, "Robonaut: Nasa's space humanoid," *Humanoid Robotics IEEE Intelligent Systems*, vol. 15, no. 4, pp. 57–63, July/August 2000.

[3] P. Beater, *Pneumatic Drives - System Design, Modelling and Control.* Berlin: Springer, 2006.

[4] J. Cui, S. Tosunoglu, R. Roberts, C. Moore, and D. W. Repperger, "A review of teleoperation system control," in *Proceedings of the Florida Conference on Recent Advances in Robotics (FCRAR)*, Boca Raton, Florida, USA, May 2003, pp. 1–12.

[5] W. R. Ferrell and T. B. Sheridan, "Supervisory control of remote manipulation," *IEEE Spectrum*, vol. 4, no. 10, pp. 81–88, October 1967.

[6] A. Filippov, "Existence and general properties of solutions of discontinuous systems," in *Differential Equations with Discontinuous Righthand Sides.* Norwell, Massachusetts 02061: Kluwer Academic Publishers, 1988, pp. 48–122.

[7] A. Girin, F. Plestan, X. Brun, and A. Glumineau, "High-order sliding-mode controllers of an electropneumatic actuator: Application to an aeronautic benchmark," *International Journal of Control*, vol. 79, no. 2, pp. 119–131, 2006.

[8] E. Hempel, H. Fischer, L. Gumb, T. Höhn, H. Krause, U. Voges, H. Breitwieser, B. Gutmann, J. Durke, M. bock, and A. Melzer, "An MRI-compatible surgical robot for precise radiological interventions," *Computer Aided Surgery*, vol. 8, no. 4, pp. 180–191, 2003.

[9] P. F. Hokayem and M. W. Spong, "Bilateral teleoperation: An historical survey," *Automatica*, vol. 42, no. 12, pp. 2035 – 2057, 2006.

[10] H. K. Khalil, *Nonlinear Systems.* Upper Saddle River, NJ, 07458: Prentice Hall, 1996.

[11] V. Lagerburg, M. A. Moerland, M. K. Konings, R. E. van de Vosse, J. J. W. Lagendijk, and J. J. Battermann, "Development of a tapping device: a new needle insertion method for prostate brachytherapy," *Physics in Medicine and Biology*, vol. 51, no. 4, pp. 891–902, 2006.

[12] B. T. Larson, A. G. Erdman, N. V. Tsekos, E. Yacoub, P. V. Tsekos, and I. G. Koutlas, "Design of an MRI-compatible robotic stereotactic device for minimally invasive interventions in the breast," *Journal of Biomechanical Engineering*, vol. 126, no. 4, pp. 458–465, 2004.

[13] M. Le, M. Pham, R. Moreau, and T. Redarce, "Transparency of a pneumatic teleoperation system using on/off solenoid valves," in *Proceedings of 2010 19th IEEE International Symposium on Robot and Human Interactive Communication*, Viareggio, Italy, September 2010, pp. 15–20.

[14] M. Le, M. Pham, M. Tavakoli, and R. Moreau, "Sliding mode control of a pneumatic haptic teleoperation system with on/off solenoid valves," in *Proceedings of 2011 IEEE International Conference on Robotics and Automation (ICRA)*, Shanghai, China, May 2011.

[15] H. K. Lee, G. S. Choi, and G. H. Choi, "A study on tracking position control of pneumatic actuators," *Mechatronics*, vol. 12, no. 6, pp. 813–831, 2002.

[16] M. Li, D. Mazilu, and K. A. Horvath, "Robotic system for transapical aortic valve replacement with MRI guidance," in *Proceedings of 2008 International Conference on Medical Image Computing and Computer-Assisted Intervention*, New York, United States, September 2008, pp. 476–484.

[17] A. Messina, N. I. Giannoccaro, and A. Gentile, "Experimenting and modelling the dynamics of pneumatic actuators controlled by the pulse width modulation (PWM) technique," *Mechatronics*, vol. 15, no. 7, pp. 859–881, 2005.

[18] T. Nguyen, J. Leavitt, F. Jabbari, and J. E. Bobrow, "Accurate sliding-mode control of pneumatic systems using low-cost solenoid valves," *IEEE/ASME Transactions on Mechatronics*, vol. 12, no. 2, pp. 216–219, 2007.

[19] G. Niemeyer, C. Preusche, and G. Hirzinger, "Telerobotics," in *Springer Handbook of Robotics*, B. Siciliano and O. Khatib, Eds. Berlin Heidelberg, Germany: Springer-Verlag, 2008, pp. 741–757.

[20] R. Oboe and P. Fiorini, "A design and control environment for internet-based telerobotics," *International Journal of Robotics Research*, vol. 17, no. 4, pp. 433–449, April 1998.

[21] M. Oura, Y. Kobayashi, J. Okamoto, and M. Fujie, "Development of MRI compatible versatile manipulator for minimally invasive surgery," in *Proceedings of 2006 First IEEE/RAS-EMBS International Conference on Biomedical Robotics and Biomechatronics*, Tuscany, Italy, Febuary 2006, pp. 176–181.

[22] J. H. Park and H. C. Cho, "Sliding-mode controller for bilateral teleoperation with varying time delay," in *Proceedings of IEEE/ASME International Conference on Advanced Intelligent Mechatronics*, Atlanta, USA, September 1999, pp. 311–316.

[23] D. Petrisor, M. Muntener, D. Mazilu, M. Schär, and D. Stoianovici, "Automatic brachytherapy seed placement under MRI guidance," *IEEE Transactions on Biomedical Engineering*, vol. 54, no. 8, pp. 1499–1506, 2007.

[24] L. Potters, C. Morgenstern, E. Calugaru, P. Fearn, A. Jassal, J. Presser, and E. Mullen, "12-year outcomes following permanent prostate brachytherapy in patients with clinically localized prostate cancer," *The Journal of Urology*, vol. 173, no. 5, pp. 1562–1566, 2005.

[25] J. A. Rosas-Flores, J. A. Flores-Campos, and L. G. Corona-Ramírez, "Optimal linearization of the dynamic behavior of an on/off actuated single pneumatic cylinder," in *Proceedings of 2008 5th International Conference on Electrical Engineering, Computing Science and Automatic Control (CCE 2008)*, Mexico City, November 2008, pp. 380–385.

[26] S. Ross, R. Waliany, and M. Swanson, "Inverse kinematics and balance control for intuitive teleoperation of a six-legged mining robot," Robotics Institute, Carnegie Mellon University, Tech. Rep., May 2009.

[27] A. Sabanovic, L. M. Fridman, and S. Spurgeon, *Variable Structure Systems: from principles to implementation.* London, United Kingdom: The Institution of Engineering and Technology, 2004.

[28] J. M. Sabater, M. Hernandez, R. J. Saltarén, R. Aracil, E. Yime, and J. M. Azorín, "Teleoperated parallel climbing robots in nuclear installations," *Industrial Robot: An International Journal*, vol. 33, no. 5, pp. 381–386, September 2006.

[29] X. Shen, J. Zhang, E. J. Barth, and M. Goldfarb, "Nonlinear model-based control of pulse width modulated pneumatic servo systems," *Journal of Dynamic Systems, Measurement, and Control*, vol. 128, pp. 663–669, 2006.

[30] T. B. Sheridan, "Telerobotics," *Automatica*, vol. 25, no. 4, pp. 487–507, July 1989.

[31] M.-C. Shih and M.-A. Ma, "Position control of a pneumatic cylinder using fuzzy PWM control method," *Mechatronics*, vol. 8, no. 3, pp. 241–253, 1998.

[32] J.-J. E. Slotine and W. Li, "Sliding control," in *Applied Nonlinear Control*. Englewood Cliffs, New Jersey 07632: Prentice Hall, 1991, pp. 276–310.

[33] M. Taghizadeh, A. Ghaffari, and F. Najafi, "Improving dynamic performances of PWM-driven servo-pneumatic systems via a novel pneumatic circuit," *ISA Transactions*, 2009.

[34] M. Tavakoli, A. Aziminejad, R. Patel, and M. Moallem, "High-fidelity bilateral teleoperation systems and the effect of multimodal haptics," *IEEE Transactions on Systems, Man and Cybernetics – Part B*, vol. 37, no. 6, pp. 1512–1528, December 2007.

[35] M. Uecker, S. Zhang, D. Voit, A. Karaus, K.-D. Merboldt, and J. Frahm, "Real-time MRI at a resolution of 20 ms," *NMR in Biomedicine*, vol. 23, no. 8, pp. 986–994, 2010.

[36] V. I. Utkin, "Sliding mode control design principles and applications to electric drives," *IEEE Transactions on Industrial Electronics*, vol. 40, no. 1, pp. 23–36, 1993.

[37] V. I. Utkin and H.-C. Chang, "Sliding mode control on electro-mechanical systems," *Mathematical Problems in Engineering*, vol. 8, no. 4-5, pp. 451–473, 2002.

[38] K. Xing, J. Huang, Y. Wang, J. Wu, Q. Xu, and J. He, "Tracking control of pneumatic artificial muscle actuators based on sliding mode and non-linear disturbance observer," *IET Control Theory and Applications*, vol. 4, no. 10, pp. 2058–2070, 2010.

[39] T. Yoshikawa and Y. Ichinoo, "Impedance identification of human fingers using virtual task environment," in *Proceedings of IEEE/RSJ International Conference on Intelligent Robots and Systems (IROS)*, Los Vegas, Nevada, USA, October 2003.

[40] K. D. Young, V. I. Utkin, and Ümit Özgüner, "A control engineer's guide to sliding mode control," *IEEE Transactions on Control Systems Technology*, vol. 7, no. 3, pp. 328–342, May 1999.

[41] N. Yu, C. Hollnagel, A. Blickenstorfer, S. S. Kollias, and R. Riener, "Comparison of MRI-compatible mechatronic systems with hydrodynamic and pneumatic actuation," *IEEE/ASME Transactions on Mechatronics*, vol. 13, no. 3, pp. 268–277, 2008.